

Phase-field modeling of eutectic solidification

Seong Gyoon Kim^{a,*}, Won Tae Kim^b, Toshio Suzuki^c, Machiko Ode^d

^aDepartment of Materials Science and Engineering, Kunsan National University, Kunsan 573-701, South Korea

^bDivision of Applied Science, Chongju University, Chongju 360-764, South Korea

^cDepartment of Materials Science and Engineering, The University of Tokyo, Tokyo 113, Japan

^dGraduate School, The University of Tokyo, Tokyo 113, Japan

Received 22 March 2002; accepted 20 August 2003

Communicated by G.B. McFadden

Abstract

We present a eutectic phase-field model, developed by extending the interface field method (Steinbach and Pezzolla, *Physica D* 134 (1999) 385) under a condition that coexisting phases at a given point have an equal chemical potential difference between solute atom and solvent atom. Also an anisotropic eutectic phase-field equation is derived explicitly. The equilibrium interface geometries, calculated using the isotropic and anisotropic models, at a triple junction under a thermal gradient are in good agreement with the exact solutions, indicating the maintenance of mechanical equilibrium at the junction. The model successfully reproduces a variety of eutectic lamellar patterns observed in experiments on directional solidification of thin film $\text{CBr}_4\text{--C}_2\text{Cl}_6$ organic alloys, under the real experimental conditions without any fitting parameters. Most of the characteristics of the pattern change with lamellar spacing in both eutectic and hypereutectic alloys are in good agreement with experimental observations.

© 2003 Elsevier B.V. All rights reserved.

PACS: 64.70.Dv; 81.30.Fb; 81.10.Aj; 05.70.Ln

Keywords: A1. Directional solidification; A1. Eutectics; A1. Growth models; A1. Morphological stability

1. Introduction

The evolution of interface pattern during solidification has been an attractive but difficult subject in science and technology societies. Predicting solidification microstructure in alloys, which is controlling their final physical and chemical properties, is important from the en-

gineering point of view. The classical sharp interface model has been used extensively to simulate the pattern evolution. In the model, diffusion equations are solved in both liquid and solid phases with imposed boundary conditions at the interface. Therefore tracking of interface position is required at every time step, which prevents its application into a rather complex pattern geometry or 3D simulation.

During last decade, a phase-field approach has been developed to solve this problem in simulating the solidification pattern evolution [1–13]. In the

*Corresponding author. Tel.: +82-63-469-4732; fax: +82-63-469-4731.

E-mail address: sgkim@kunsan.ac.kr (S. Gyoon Kim).

phase-field models (PFMs), the phase field ϕ is introduced to describe the distribution of solid, liquid and interface in the whole system. The interface is assumed to be thin but finite in width, over which the phase field ϕ changes smoothly from $\phi = 0$ in liquid region to $\phi = 1$ in solid region. The equations governing the phase field and diffusion field are derived in a natural way from a definition of the free energy functional of the system, which is decreasing monotonically with time. The governing equations are written as unified ones in the whole space of the system, which makes us to circumvent the tedious and difficult process of interface tracking during computation. Especially the asymptotic analysis at the thin interface limit [11–13] greatly enhanced the computational efficiency of the phase-field simulation.

The original PFMs for single phase solidification [1–13] in pure or alloy melts have been extended to multiphase system by several groups [14–23]. Most approaches [14–21] assume implicitly that any point within the interfacial region is a mixture of solid and liquid phases with an equal composition. Due to the assumption, at the interface there is not only intentionally imposed double well potential but also an extra chemical double-well potential contributing to interface energy [10,24]. If the width of the interface is increased for high computational efficiency, the excess energy from the extra potential can be larger than the material's interfacial energy itself. Therefore there is a restriction on the interface width [10,24], which prevent us from computing under usual experimental conditions, as will be shown in Appendix A. Several simulations [17–21] for multiphase systems adopt the spinodal decomposition at the interface. In these approaches, the nucleations of the second phases take place spontaneously when the lamellar spacing λ is significantly larger than λ_m (the spacing corresponding to the minimum undercooling). The maximum spacing that can be simulated without nucleation seems to be less than $2.2\lambda_m$ [21]. However, the experiments [25–28] on the directional eutectic solidification in 2D geometry showed no nucleation of the second phase during growth. When the initial lamellar spacing is much

larger than λ_m , tilting or oscillating instability takes place instead of the nucleation of new lamella phase.

Recently Steinbach and Pezzolla [29] introduced an interface field concept, defined between two phases at the interfacial region, and reformulated the previously developed multiphase PFM [22,23]. With the interface field variable, the changes of physical quantities at a triple junction region can be decomposed into a sum of contributions from three independent interface fields. In this study, we develop a phase-field model of eutectic solidification by using the interface-field method and a new condition of the equal chemical potential among the coexisting phases. The latter has been adopted in a previous study to remove the extra chemical double-well potential at the interfacial region [10]. We use this model to simulate a variety of lamella eutectic patterns observed in directional solidification of thin film $\text{CBr}_4\text{--C}_2\text{Cl}_6$ organic alloys under the real experimental conditions without any fitting parameters.

It should be mentioned that standard PFMs for alloy solidification have suffered from the anomalous interfacial effects such as the chemical potential jump at the interface, enhanced interface diffusion and interface stretching [30]. Even though the anomalous effects become negligible at the sharp interface limit condition, they can give influences on the dynamics of interface in usual computation condition having a finite interface width. Recently Karma [31] presented a method to eliminate all the anomalous effects by adding an anti-trapping mass current term to the diffusion equation. However, the extension of the model to multi-phase system is not straightforward. In this eutectic phase field model, therefore, we will follow our previous approach [10] where the phase-field mobility is determined with a correction due to a finite interface width, but the anomalous chemical potential jump and interface diffusion remains. In Section 2.6 and Appendix B, instead, we will discuss quantitatively their possible relevance to the computations.

This paper is organized as follows: In Section 2, we first derive isotropic phase-field and diffusion equations for eutectic solidification by using the interface-field method and the equal chemical

potential condition. Next we derive anisotropic multiphase-field equation. Also we present the relationships between thermodynamic variables and parameters in eutectic phase diagram, such as liquidus slope, eutectic composition, eutectic temperature, partition coefficient. Finally the relationship between the phase-field mobility and interface kinetics coefficient is derived at 1D thin interface limit condition. In Section 3, computation methods are described in details. In the final Section 4, the maintenance of mechanical equilibrium at a triple junction is tested by comparing the computation results on the equilibrium interface shapes at the grain boundary groove under a thermal gradient with corresponding exact solutions for both isotropic and anisotropic solid–liquid interface energies. Then we show the 2D computation results on the lamella eutectic patterns in directional solidification of $\text{CBr}_4\text{--C}_2\text{Cl}_6$ organic alloys obtained under the same physical parameters and conditions with experiments [25–28]. Especially we focus on the tilt and oscillatory instability patterns as a function of lamellar spacing in the eutectic and a hypereutectic compositions, and compare the computation results directly with the experimental results. In Appendix A, we discuss the existence of the extra chemical double well-potential in the phase-field models adopting the equal composition condition and derive its explicit functional form for an alloy with straight phase boundaries in the phase diagram. Also we estimate explicitly the grid size restriction arising from the potential to show why such an approach is not suitable for simulating the eutectic solidification of $\text{CBr}_4\text{--C}_2\text{Cl}_6$ organic alloys under the real experimental conditions. In Appendix B, we discuss quantitatively the relevance of the anomalous chemical potential jump to our computations.

2. Eutectic phase-field model

In eutectic solidification, two solid phases (α, β) form from a liquid phase (L). The coexisting three phases are denoted by phase fields ϕ_i ($i = 1, 2, 3$): $\phi_1 = 1$ and $\phi_2 = \phi_3 = 0$ in α phase; $\phi_2 = 1$ and $\phi_1 = \phi_3 = 0$ in β phase; $\phi_3 = 1$ and $\phi_1 = \phi_2 = 0$

in L phase. The sum of each phase fields at any position in the system is conserved;

$$\sum_{i=1}^3 \phi_i = 1. \quad (2.1)$$

The free energy functional of a system of volume V is given by

$$F = \int_V \left[f^P + f^T + \lambda_L \left(\sum_i \phi_i - 1 \right) \right] dV, \quad (2.2)$$

where λ_L is the Lagrange multiplier accounting for the constraint (2.1), and f^P can be defined by

$$f^P = \sum_{j>i} \sum_i \left[-\frac{\varepsilon_{ij}^2}{2} \nabla \phi_i \cdot \nabla \phi_j + \omega_{ij} \phi_i \phi_j \right] \quad (2.3)$$

as in Steinbach and Pezzolla [29], where ε_{ij} is the gradient energy coefficient and ω_{ij} is the height of the double well potential. The parabolic double-well potential $\phi_i \phi_j$ is defined in the interfacial region only where $0 < \phi_i < 1$ and $0 < \phi_j < 1$. For the thermodynamic potential f^T , we assume a rule of mixture

$$f^T = \sum_i \phi_i f^i(c_i), \quad (2.4)$$

where $f^i(c_i)$ is the free energy density of i phase with composition c_i . Any point (x, t) in the system is assumed to be a mixture of three phases, with the fraction of ϕ_i for i phase. However, the compositions of the phases coexisting at a given point are not independent of each other, but constrained by a following condition [10]:

$$f_{c_1}^1[c_1(x, t)] = f_{c_2}^2[c_2(x, t)] = f_{c_3}^3[c_3(x, t)] \equiv f_c(x, t), \quad (2.5)$$

where the subscripts c_i under the free energy densities denote the derivatives by them. This condition enforces the coexisting phases to have an equal chemical potential, which is defined by the difference of chemical potential between solute and solvent. In several PFMs [14–21], in contrast with Eq. (2.5), the coexisting phases at a point were assumed implicitly to have an equal composition ;

$$c_1(x, t) = c_2(x, t) = c_3(x, t) \equiv c. \quad (2.6)$$

With the imposed equal chemical potential condition (2.5), instead of the condition (2.6), the extra chemical double well potential at the interfacial region can be removed [10], resulting in a relaxation of interface width limitation. This will be explained in detail in Appendix A. Average composition of the mixture also is given by a mixture rule

$$c(x, t) = \sum_i \phi_i c_i. \quad (2.7)$$

With the restrictions of Eqs. (2.1), (2.5) and (2.7), the compositions c_i ($i = 1, 2, 3$) of each phase can be expressed as functions of c and ϕ_i .

2.1. Phase-field equation

We define a step function $s_i(x, t) = 1$ if $\phi_i > 0$ and $s_i(x, t) = 0$ otherwise. Then the number of phases coexisting in a given point can be written as

$$n(x, t) = \sum_{i=1}^3 s_i(x, t). \quad (2.8)$$

Following Ref. [29], we introduce the interface field ψ_{ij} as

$$\psi_{ij} = \phi_i - \phi_j, \quad (2.9)$$

which is defined only within the interfacial region where $s_i \neq 0$ and $s_j \neq 0$. We then can write an identity

$$\phi_i = \frac{1}{n} \left(\sum_{j \neq i} s_{ij} \psi_{ij} + 1 \right) \quad (2.10)$$

with the notation $s_{ij} = s_i s_j$. It then follows

$$\frac{\partial \phi_i}{\partial t} = \frac{1}{n} \sum_{j \neq i} s_{ij} \frac{\partial \psi_{ij}}{\partial t} = \frac{1}{n} \sum_{j \neq i} s_{ij} \left(\frac{\partial \phi_i}{\partial t} - \frac{\partial \phi_j}{\partial t} \right). \quad (2.11)$$

Note that the change of the phase-field takes place only in the interfacial region where s_{ij} is not vanishing. Eq. (2.11) indicates that phase-field change at a given point can be decomposed into a sum of interface field changes at the point [29]. For example when $i = 1$, the change in the phase field ϕ_1 is attributed to the motions of the 1–2 interface and 1–3 interface. We then make the

relaxation ansatz

$$\frac{\partial \phi_i}{\partial t} - \frac{\partial \phi_j}{\partial t} = -2M_{ij} \left[\frac{\delta F}{\delta \phi_i} - \frac{\delta F}{\delta \phi_j} \right]. \quad (2.12)$$

With definitions (2.3) and (2.4), the functional derivatives in Eq. (2.12) are given by

$$\frac{\delta F}{\delta \phi_i} = \frac{\delta F^P}{\delta \phi_i} + \frac{\delta F^T}{\delta \phi_i} - \lambda_L. \quad (2.13)$$

The first term in the righthand side of Eq. (2.13) is given by

$$\frac{\delta F^P}{\delta \phi_i} = \sum_{j \neq i} \left[\frac{\varepsilon_{ij}^2}{2} \nabla^2 \phi_j + \omega_{ij} \phi_j \right]. \quad (2.14)$$

Eqs. (2.8)–(2.14) are the same ones as in Ref. [29]. With the thermodynamic potential Eq. (2.4) and the equal chemical potential condition (2.5), the second term in the righthand side of Eq. (2.13) becomes

$$\begin{aligned} \frac{\delta F^T}{\delta \phi_i} &= f^i(c_i) + \sum_j \phi_j f_{c_j}^j(c_j) \frac{\partial c_j}{\partial \phi_i} \\ &= f^i(c_i) + f_c \sum_j \phi_j \frac{\partial c_j}{\partial \phi_i}, \end{aligned} \quad (2.15)$$

where we used condition (2.5). Differentiating Eq. (2.7) with ϕ_i yields

$$c_i + \sum_j \phi_j \frac{\partial c_j}{\partial \phi_i} = 0 \quad (2.16)$$

and then we get

$$\frac{\delta F^T}{\delta \phi_i} = f^i(c_i) - c_i f_c. \quad (2.17)$$

Using Eqs. (2.11)–(2.17), we find the phase-field equation

$$\frac{\partial \phi_i}{\partial t} = -\frac{2}{n} \sum_{j \neq i} s_{ij} M_{ij} \left[\frac{\delta F}{\delta \phi_i} - \frac{\delta F}{\delta \phi_j} \right], \quad (2.18)$$

where

$$\frac{\delta F}{\delta \phi_i} = \sum_{j \neq i} \left[\frac{\varepsilon_{ij}^2}{2} \nabla^2 \phi_j + \omega_{ij} \phi_j \right] + f^i(c_i) - c_i f_c \quad (2.19)$$

with $\omega_{ij} = \omega_{ji}$ and $\varepsilon_{ij} = \varepsilon_{ji}$. Note that Lagrange multiplier was cancelled out in Eq. (2.18) and so we omitted it in Eq. (2.19). It should be emphasized that Eq. (2.19) was derived under the

condition of the equal chemical potential among the coexisting phases, given by Eq. (2.5).

2.2. Diffusion equation

The diffusion equation where the mass should be conserved is written as

$$\frac{\partial c}{\partial t} = \nabla M_c \nabla \frac{\delta F}{\delta c}, \quad (2.20)$$

where M_c is the mobility of the diffusion field. The derivative can be modified into

$$\frac{\delta F}{\delta c} = \sum_i \phi_i f_c^i(c_i) \frac{\partial c_i}{\partial c} = f_c \sum_i \phi_i \frac{\partial c_i}{\partial c} = f_c, \quad (2.21)$$

where we used Eq. (2.2), condition (2.5) and $\sum \phi_i \partial c_i / \partial c = 1$ from Eq. (2.7). If we put $M_c = D/f_{cc}$, where D is the diffusivity dependent on the phase fields, then the diffusivity in a bulk phase can be maintained as a constant and the diffusion equation (2.20) becomes

$$\begin{aligned} \frac{\partial c}{\partial t} &= \nabla \frac{D}{f_{cc}} \nabla f_c \\ &= \nabla D \nabla c + \nabla \cdot \frac{D}{f_{cc}} \sum_i f_{c\phi_i} \nabla \phi_i. \end{aligned} \quad (2.22)$$

With the relationship $f_{c\phi_i}/f_{cc} = -c_i$ which can be easily derived from Eqs. (2.5) and (2.7), we find

$$\frac{\partial c}{\partial t} = \nabla \cdot D \nabla c - \nabla \cdot D \sum_i c_i \nabla \phi_i. \quad (2.23)$$

By using Eq. (2.7) again, this equation may be written as an equivalent, but more compact and convenient form

$$\frac{\partial c}{\partial t} = \nabla \cdot D \sum_i \phi_i \nabla c_i. \quad (2.24)$$

2.3. Parameters in phase-field equation

In order to find the relationships between the phase-field parameters and materials' parameters, we consider an equilibrium state having a flat boundary between α ($\phi_1 = 1$) at $x < 0$ and L

($\phi_3 = 1$) at $x > 0$;

$$\begin{aligned} \varepsilon_{13}^2 \frac{d^2 \phi_1}{dx^2} - \omega_{13}(1 - 2\phi_1) - [f^1(c_1) - f^3(c_3) \\ - (c_1 - c_3)f_c] = 0, \end{aligned} \quad (2.25)$$

$$\frac{d}{dx} D \left[\phi_1 \frac{dc_1}{dx} + (1 - \phi_1) \frac{dc_3}{dx} \right] = 0 \quad (2.26)$$

with the conditions

$$f_c^1[c_1(x, t)] = f_c^3[c_3(x, t)] \equiv f_c(x, t), \quad (2.27)$$

$$c(x, t) = \phi_1 c_1 + \phi_3 c_3, \quad (2.28)$$

where $\phi_1 + \phi_3 = 1$. For the stationary interface, Eq. (2.26) yields $c_1 = c_1^e$ (constant) and $c_3 = c_3^e$ (constant), which is equivalent to

$$f_c^1(c_1^e) = f_c^3(c_3^e) = f_c^e = \text{constant} \quad (2.29)$$

due to condition (2.27). Therefore the phase-field equation (2.25) at equilibrium state is

$$\begin{aligned} \varepsilon_{13}^2 \frac{d^2 \phi_1}{dx^2} - \omega_{13}(1 - 2\phi_1) - [f^1(c_1^e) - f^3(c_3^e) \\ - f_c^e(c_1^e - c_3^e)] = 0. \end{aligned} \quad (2.30)$$

Integrating this equation combined with Eq. (2.29), under the conditions $\phi_1 = 1$ at $x = -\infty$ and $\phi_1 = 0$ at $x = \infty$ reproduces the well-known common tangent rule

$$f_c^1(c_1^e) = f_c^3(c_3^e) = \frac{f^3(c_3^e) - f^1(c_1^e)}{c_3^e - c_1^e}. \quad (2.31)$$

Also inserting Eq. (2.31) into Eq. (2.30) gives

$$\varepsilon_{13}^2 \frac{d^2 \phi_1}{dx^2} = \omega_{13}(1 - 2\phi_1) \quad (2.32)$$

and then we get the stationary phase-field profile satisfying $\phi_1 = 1/2$ at $x = 0$;

$$\phi_1 = \frac{1}{2} \left(1 - \sin \frac{\sqrt{2\omega_{13}} x}{\varepsilon_{13}} \right). \quad (2.33)$$

It should be noted that solution (2.33) is valid only within a range

$$|x| \leq \frac{\pi \varepsilon_{13}}{2\sqrt{2\omega_{13}}}. \quad (2.34)$$

This clear cut for the interfacial region enables us not only to make a definition of the step function $s_i(x, t)$, but also to take the interface width 2ξ in a

natural way as

$$2\xi = \pi \frac{\varepsilon_{13}}{\sqrt{2\omega_{13}}}. \quad (2.35)$$

The interface energy σ_{13} then is given by

$$\sigma_{13} = \varepsilon_{13}^2 \int_{-\infty}^{+\infty} \left(\frac{d\phi_1}{dx} \right)^2 dx = \frac{\pi}{8} \varepsilon_{13} \sqrt{2\omega_{13}}. \quad (2.36)$$

Parameters ε_{ij} and ω_{ij} in the phase-field equation can be found from relationships (2.35) and (2.36) for given interface energy σ_{ij} and interface width 2ξ . The relationship between the phase-field mobility M_{ij} and the interface kinetics coefficient β_{ij} will be given in the final part of this section.

2.4. Anisotropic phase-field equation

We extend the isotropic model to the case with anisotropies in the interface energy σ_{ij} and kinetics coefficient β_{ij} , that is, $\sigma_{ij} = \sigma(\theta_i, \theta_j)$ and $\beta_{ij} = \beta_{ij}(\theta_i, \theta_j)$, where θ_i and θ_j are the angles between the x -axis and the directions normal to the $\phi_i = \text{constant}$ and $\phi_j = \text{constant}$ lines, respectively;

$$\theta_i = \tan^{-1} \frac{(\phi_i)_y}{(\phi_i)_x}. \quad (2.37)$$

Throughout this section, the subscripts under the parentheses denote the partial derivatives by them. Following a similar procedure as in the previous treatments [5,9], we put $\varepsilon_{ij} = \varepsilon_{ij}(\theta_i, \theta_j)$ and $M_{ij} = M_{ij}(\theta_i, \theta_j)$. Because the orientation dependence of the phase-field mobility can be easily treated, we here focus on the gradient coefficient $\varepsilon_{ij} = \varepsilon_{ij}(\theta_i, \theta_j)$. For convenience, we introduce an average orientation

$$\theta_{ij} = \frac{1}{2}(\theta_i + \theta_j). \quad (2.38)$$

If we assume both ε_{ij} and M_{ij} to be functions of θ_{ij} , that is,

$$\varepsilon_{ij} = \varepsilon_{ij}(\theta_{ij}), \quad (2.39)$$

$$M_{ij} = M(\theta_{ij}), \quad (2.40)$$

then it follows

$$(\varepsilon_{ij})_{\theta_i} = (\varepsilon_{ij})_{\theta_j} = \frac{1}{2} \frac{d\varepsilon_{ij}(\theta_{ij})}{d\theta_{ij}} \equiv \frac{1}{2} \varepsilon'_{ij}, \quad (2.41)$$

$$(\varepsilon_{ij})_{\theta_i, \theta_i} = (\varepsilon_{ij})_{\theta_j, \theta_j} = \frac{1}{4} \frac{d^2 \varepsilon_{ij}(\theta_{ij})}{d\theta_{ij}^2} \equiv \frac{1}{4} \varepsilon''_{ij}. \quad (2.42)$$

For simplicity, we consider a part of the functional (2.2);

$$F_{ij} = - \int_V \left[\frac{\varepsilon_{ij}^2(\theta_{ij})}{2} \nabla \phi_i \cdot \nabla \phi_j \right] dV. \quad (2.43)$$

The variation $\delta\phi_i$ in the phase field ϕ_i yields the variation of the functional

$$\begin{aligned} \delta F_{ij} &= - \delta \int_V \frac{\varepsilon_{ij}^2(\theta_{ij})}{2} \nabla \phi_i \cdot \nabla \phi_j dV \\ &= - \int_V \varepsilon_{ij} \delta \varepsilon_{ij} \nabla \phi_i \cdot \nabla \phi_j dV \\ &\quad - \int_V \frac{\varepsilon_{ij}^2}{2} \nabla \delta \phi_i \cdot \nabla \phi_j dV \\ &= - \int_V \varepsilon_{ij} \delta \varepsilon_{ij} \nabla \phi_i \cdot \nabla \phi_j dV \\ &\quad + \frac{1}{2} \int_V \delta \phi_i \nabla \cdot (\varepsilon_{ij}^2 \nabla \phi_j) dV. \end{aligned} \quad (2.44)$$

The variation $\delta \varepsilon_{ij}$ due to $\delta \phi_i$ in the first integral in Eq. (2.44) can be modified as

$$\delta \varepsilon_{ij} = (\varepsilon_{ij})_{\theta_i} \delta \theta_i = \frac{\varepsilon'_{ij}}{2|\nabla \phi_i|^2} [(\phi_i)_x (\delta \phi_i)_y - (\phi_i)_y (\delta \phi_i)_x]. \quad (2.45)$$

The first integral in Eq. (2.44) then can be written as

$$\begin{aligned} &\int_V \varepsilon_{ij} \delta \varepsilon_{ij} \nabla \phi_i \cdot \nabla \phi_j dV \\ &= \int_V \frac{\varepsilon_{ij} \varepsilon'_{ij}}{2} \frac{\nabla \phi_i \cdot \nabla \phi_j}{|\nabla \phi_i|^2} [(\phi_i)_x (\delta \phi_i)_y - (\phi_i)_y (\delta \phi_i)_x] dV \\ &= -\frac{1}{2} \int_V \frac{\partial}{\partial y} \left[\varepsilon_{ij} \varepsilon'_{ij} \frac{\nabla \phi_i \cdot \nabla \phi_j}{|\nabla \phi_i|^2} (\phi_i)_x \right] \delta \phi_i dV \\ &\quad + \frac{1}{2} \int_V \frac{\partial}{\partial x} \left[\varepsilon_{ij} \varepsilon'_{ij} \frac{\nabla \phi_i \cdot \nabla \phi_j}{|\nabla \phi_i|^2} (\phi_i)_y \right] \delta \phi_i dV. \end{aligned} \quad (2.46)$$

We then obtain the functional derivative

$$\frac{\delta F_{ij}}{\delta \phi_i} = \nabla \cdot \left(\frac{\varepsilon_{ij}^2}{2} \nabla \phi_j \right) + \frac{1}{2} \frac{\partial}{\partial y} [\varepsilon_{ij} \varepsilon'_{ij} (\phi_i)_x P_{ij}] - \frac{1}{2} \frac{\partial}{\partial x} [\varepsilon_{ij} \varepsilon'_{ij} (\phi_i)_y P_{ij}], \quad (2.47)$$

where we defined

$$P_{ij} \equiv \nabla \phi_i \cdot \nabla \phi_j / |\nabla \phi_i|^2. \quad (2.48)$$

In order to modify the derivative into the more convenient form, we note

$$\begin{aligned} \nabla \cdot \left(\frac{\varepsilon_{ij}^2}{2} \nabla \phi_j \right) &= \frac{\varepsilon_{ij}^2}{2} \nabla^2 \phi_j + \varepsilon_{ij} \nabla \varepsilon_{ij} \cdot \nabla \phi_j \\ &= \frac{\varepsilon_{ij}^2}{2} \nabla^2 \phi_j + \varepsilon_{ij} \varepsilon'_{ij} \nabla \theta_{ij} \cdot \nabla \phi_j. \end{aligned} \quad (2.49)$$

Then Eq. (2.47) can be written as

$$\begin{aligned} \frac{\delta F_{ij}}{\delta \phi_i} &= \frac{\varepsilon_{ij}^2}{2} \nabla^2 \phi_j + \varepsilon_{ij} \varepsilon'_{ij} [\nabla \theta_{ij} \cdot \nabla \phi_j \\ &\quad + \frac{1}{2} (\phi_i)_x (P_{ij})_y - \frac{1}{2} (\phi_i)_y (P_{ij})_x] + \frac{1}{2} [(\varepsilon'_{ij})^2 \\ &\quad + \varepsilon_{ij} \varepsilon''_{ij}] P_{ij} [(\theta_{ij})_y (\phi_i)_x - (\theta_{ij})_x (\phi_i)_y]. \end{aligned} \quad (2.50)$$

One may use the Eq. (2.47) or Eq. (2.50) directly for simulation. In such case, however, we can hardly maintain the same second order accuracy for all the terms in the right hand side of Eq. (2.47) or Eq. (2.50) because of the partial derivatives of P_{ij} and θ_{ij} . Therefore it is necessary to expand explicitly the partial derivatives of P_{ij} and θ_{ij} in order to maintain the second order accuracy in the difference equation. Because the expansion procedure is rather lengthy in algebra, here we present only the final result;

$$\frac{\delta F_{ij}}{\delta \phi_i} = \frac{1}{2} \varepsilon_{ij}^2 \nabla^2 \phi_j + \frac{1}{2} \varepsilon_{ij} \varepsilon'_{ij} B_{ij} + \frac{1}{2} [(\varepsilon'_{ij})^2 + \varepsilon_{ij} \varepsilon''_{ij}] A_{ij}, \quad (2.51)$$

where A_{ij} and B_{ij} are defined by

$$\begin{aligned} A_{ij} &= \frac{P_{ij}}{4} [\nabla^2 \phi_i + [(\phi_i)_{yy} - (\phi_i)_{xx}] \cos 2\theta_i \\ &\quad - 2(\phi_i)_{xy} \sin 2\theta_i] \\ &\quad + \frac{1}{8} (1 + \cos 2\theta_i \cos 2\theta_j + \sin 2\theta_i \sin 2\theta_j) \nabla^2 \phi_j \end{aligned}$$

$$\begin{aligned} &+ \frac{1}{8} (\cos 2\theta_i + \cos 2\theta_j) [(\phi_j)_{yy} - (\phi_j)_{xx}] \\ &- \frac{1}{4} (\sin 2\theta_i + \sin 2\theta_j) (\phi_j)_{xy}, \end{aligned} \quad (2.52)$$

$$\begin{aligned} B_{ij} &= W_{ij} [\nabla^2 \phi_i + [(\phi_i)_{yy} - (\phi_i)_{xx}] \cos 2\theta_i - 2(\phi_i)_{xy} \sin 2\theta_i] \\ &\quad + \frac{1}{2} (\sin 2\theta_j + \sin 2\theta_i) [(\phi_j)_{yy} - (\phi_j)_{xx}] \\ &\quad + (\cos 2\theta_j + \cos 2\theta_i) (\phi_j)_{xy}, \end{aligned} \quad (2.53)$$

$$W_{ij} = \frac{(\phi_j)_y (\phi_i)_x - (\phi_j)_x (\phi_i)_y}{|\nabla \phi_i|^2}, \quad (2.54)$$

$$P_{ij} = \frac{(\phi_j)_x (\phi_i)_x + (\phi_j)_y (\phi_i)_y}{|\nabla \phi_i|^2}. \quad (2.55)$$

Therefore we find the anisotropic phase-field equation

$$\frac{\partial \phi_i}{\partial t} = -\frac{2}{n} \sum_{j \neq i} s_{ij} M_{ij}(\theta_i, \theta_j) \left[\frac{\delta F^a}{\delta \phi_i} - \frac{\delta F^a}{\delta \phi_j} \right], \quad (2.56)$$

where the functional derivatives are given by

$$\begin{aligned} \frac{\delta F^a}{\delta \phi_i} &= \frac{1}{2} \sum_{j \neq i} \left[\varepsilon_{ij}^2 \nabla^2 \phi_j + \varepsilon_{ij} \varepsilon'_{ij} B_{ij} \right. \\ &\quad \left. + (\varepsilon_{ij}^2 + \varepsilon_{ij} \varepsilon''_{ij}) A_{ij} + 2\omega_{ij} \phi_j \right] + f'(c_i) - c_i f_c, \end{aligned} \quad (2.57)$$

with the same definitions for A_{ij} and B_{ij} with Eqs. (2.52) and (2.53).

Eqs. (2.56) and (2.57) recover the corresponding anisotropic equation derived for two phases interface by Warren and Boettinger [9]. We consider the interface between solid α ($\phi_1 = 1$) and liquid L ($\phi_3 = 1$) phases, where $\phi_1 + \phi_3 = 1$. In this case we get $W_{13} = W_{31} = 0$, $P_{13} = P_{31} = -1$, $\theta_1 = \theta_3$ and

$$\begin{aligned} A_{13} &= -A_{31} = -\frac{1}{2} \nabla^2 \phi_1 - \frac{1}{2} [(\phi_1)_{yy} \\ &\quad - (\phi_1)_{xx}] \cos(2\theta_1) + (\phi_1)_{xy} \sin(2\theta_1), \end{aligned} \quad (2.58)$$

$$\begin{aligned} B_{13} &= -B_{31} = -2(\phi_1)_{xy} \cos(2\theta_1) \\ &\quad - [(\phi_1)_{yy} - (\phi_1)_{xx}] \sin(2\theta_1). \end{aligned} \quad (2.59)$$

Inserting Eqs. (2.58) and (2.59) into (2.57), and putting $\phi_1 = \phi$, $\theta_1 = \theta$, $\varepsilon_{13} = \varepsilon$, $\omega_{13} = \omega$, the phase-field equation becomes

$$\begin{aligned} \frac{1}{M(\theta)} \frac{\partial \phi}{\partial t} &= \varepsilon^2 \nabla^2 \phi + \varepsilon \varepsilon' [2\phi_{xy} \cos 2\theta + (\phi_{yy} - \phi_{xx}) \sin 2\theta] \end{aligned}$$

$$\begin{aligned}
& + \frac{1}{2}(\varepsilon'^2 + \varepsilon\varepsilon'')[\nabla^2\phi + (\phi_{yy} - \phi_{xx})\cos 2\theta \\
& - 2\phi_{xy}\sin 2\theta] \\
& - \omega(1 - 2\phi) - [f^1(c_1) - f^3(c_3) \\
& - (c_1 - c_3)f_c], \tag{2.60}
\end{aligned}$$

where the terms due to the anisotropy are identical with those in Warren and Boettinger [9].

2.5. Thermodynamic terms

In present phase-field model, any data base or solution models for the thermodynamic parameters may be adopted for a given alloy system. Eutectic phase diagram is characterized by the equilibrium liquidus slopes ($m_1 < 0$, $m_2 > 0$), equilibrium partition coefficients $k_1 < 1$, $k_2 > 1$, eutectic composition (c_E) and eutectic temperature (T_E). Also quantitative analysis of experimental results of directional eutectic solidification has been performed under the assumptions of constant m_1 , m_2 and constant k_1 , k_2 , at least around the eutectic temperature T_E . Thus it is useful to make a thermodynamic model of such phase diagram for the quantitative comparison of computational results with experimental results.

We assume that the linearity of the phase boundaries in the diagram stems from the temperature dependences of the chemical potentials of pure solvent A and pure solute B , (G_A^i and G_B^i , respectively), while the solvent and solute are mixed ideally. We write the chemical potentials of component A and B in the i phase of an ideal dilute solution;

$$\mu_A^i = G_A^i(T) - \frac{RT_E}{v_m}c_i, \tag{2.61}$$

$$\mu_B^i = G_B^i(T) + \frac{RT_E}{v_m}\ln c_i. \tag{2.62}$$

At the equilibrium condition between α ($\phi_1 = 1$) and L ($\phi_3 = 1$) phases, it must hold $\mu_A^1 = \mu_A^3$ and $\mu_B^1 = \mu_B^3$:

$$G_A^1(T) - \frac{RT_E}{v_m}c_{13}^e = G_A^3(T) - \frac{RT_E}{v_m}c_{31}^e, \tag{2.63}$$

$$G_B^1(T) + \frac{RT_E}{v_m}\ln c_{13}^e = G_B^3(T) + \frac{RT_E}{v_m}\ln c_{31}^e, \tag{2.64}$$

where c_{ij}^e is the composition of i phase in equilibrium with j phase at temperature T . Because all the equilibrium compositions here are linear with temperature, it follows

$$\begin{aligned}
c_{31}^e - c_{13}^e &= \frac{G_A^3(T) - G_A^1(T)}{RT_E/v_m} \\
&= \left(c_E - \frac{T_E - T}{m_1}\right)(1 - k_1), \tag{2.65}
\end{aligned}$$

$$\ln \frac{c_{13}^e}{c_{31}^e} = \frac{G_B^3(T) - G_B^1(T)}{RT_E/v_m} = \ln k_1. \tag{2.66}$$

Therefore we find

$$G_A^3(T) - G_A^1(T) = \frac{RT_E}{v_m} \left(c_E - \frac{T_E - T}{m_1}\right)(1 - k_1), \tag{2.67}$$

$$G_B^3(T) - G_B^1(T) = \frac{RT_E}{v_m} \ln k_1. \tag{2.68}$$

Following the same way, we find the β – L equilibrium condition;

$$G_A^3(T) - G_A^2(T) = \frac{RT_E}{v_m} \left(c_E - \frac{T_E - T}{m_2}\right)(1 - k_2), \tag{2.69}$$

$$G_B^3(T) - G_B^2(T) = \frac{RT_E}{v_m} \ln k_2. \tag{2.70}$$

The α – β phase boundary in the phase diagram is not independent, but fixed by the relationships (2.67)–(2.70). However it is not relevant to this study for eutectic solidification where the reaction in solid phase can be ignored. Now if we set $G_A^3(T) = 0$ and $G_B^3(T) = 0$ as a standard state, the chemical potential of each component as a function of composition c_i becomes

$$\mu_A^1 = -\frac{RT_E}{v_m} \left(c_E - \frac{T_E - T}{m_1}\right)(1 - k_1) - \frac{RT_E}{v_m}c_1, \tag{2.71}$$

$$\mu_A^2 = -\frac{RT_E}{v_m} \left(c_E - \frac{T_E - T}{m_2}\right)(1 - k_2) - \frac{RT_E}{v_m}c_2, \tag{2.72}$$

$$\mu_A^3 = -\frac{RT_E}{v_m}c_3 \tag{2.73}$$

and

$$\mu_B^1 = \frac{RT_E}{v_m} \ln \frac{c_1}{k_1}; \quad \mu_B^2 = \frac{RT_E}{v_m} \ln \frac{c_2}{k_2}; \quad \mu_B^3 = \frac{RT_E}{v_m} \ln c_3. \quad (2.74)$$

With the chemical potentials (2.71)–(2.74), the thermodynamic variables in present phase field model could be written as functions of the variables which can be obtained from the phase diagram: At first, the equal chemical potential condition (2.5) is

$$\mu_B^1 - \mu_A^1 = \mu_B^2 - \mu_A^2 = \mu_B^3 - \mu_A^3. \quad (2.75)$$

Remind that the chemical potential $f_{c_i}^i(c_i)$ in condition (2.5) was defined by the difference of chemical potential between solute and solvent. At the dilute solution limit where all compositions are close to zero, Eqs. (2.75) can be approximated as

$$\frac{c_1}{c_3} = k_1, \quad \frac{c_2}{c_3} = k_2. \quad (2.76)$$

Next, we turn to the thermodynamic term in the phase-field equation (2.19) or (2.57). Because of condition (2.5), it follows

$$\begin{aligned} f^i(c_i) - c_i f_c &= f^i(c_i) - c_i f_{c_i}^i \\ &= [\mu_A^i(1 - c_i) + \mu_B^i c_i] - c_i [\mu_B^i - \mu_A^i] \\ &= \mu_A^i \\ &= -\frac{RT_E}{v_m} \left(c_E - \frac{T_E - T}{m_i} \right) (1 - k_i) - \frac{RT_E}{v_m} c_i \end{aligned} \quad (2.77)$$

for $i = 1$ or 2 and

$$f^3(c_3) - c_3 f_c = \mu_A^3 = -\frac{RT_E}{v_m} c_3. \quad (2.78)$$

These relationships (2.76)–(2.78) will be used in the phase-field equation and diffusion equation. From Eqs. (2.77) and (2.78), it should be noted that the thermodynamic driving force for the solidification is given by the amount of supersaturation from the equilibrium concentration in liquid phase because

$$\begin{aligned} f^1(c_1) - f^3(c_3) - (c_1 - c_3) f_c &= \mu_A^1 - \mu_A^3 \\ &= -\frac{RT_E}{v_m} \left(c_E - \frac{T_E - T}{m_1} \right) (1 - k_1) - \frac{RT_E}{v_m} c_1 + \frac{RT_E}{v_m} c_3 \\ &= -(1 - k_1) \frac{RT_E}{v_m} [c_{31}^e - c_3] \end{aligned} \quad (2.79)$$

for α – L interface, where we used the relation $m_1 = (T_E - T)/(c_E - c_{31}^e)$ and $c_1 = k_1 c_3$. For β – L interface, the similar relation also holds.

Even though relationships (2.76)–(2.78) were obtained under the assumptions of straight phase boundaries in the phase diagram and dilute solution approximation, they can be applicable to a real alloy system with a general phase-diagram by taking local slopes of the phase boundaries and local partition coefficients, as long as one assumes that the thermodynamic driving force can be expressed by the amount of supersaturation from the equilibrium concentration, or equivalently by the amount of undercooling below the equilibrium temperature.

2.6. Thin interface limit

Phase-field parameters can be chosen in two different limits: a sharp interface limit having a vanishingly small interface width [5,8] and a thin interface limit having a finite interface width but much smaller than diffusion boundary layer width [11–13]. The former imposes a stringent limitation on the interface width 2ξ , which can be hardly attained in numerical computation of PFM at low undercooling because of the limited computational resources. However, the latter relaxes not only the interface width limitation, but also makes it possible to eliminate the interface kinetics effect. Karma and Rappel [11–13] showed that the PFM with a finite interface width can be mapped on the sharp interface model. The basic idea of the thin interface PFM can be seen in Fig. 1 showing the temperature profile across the planar interface moving with a velocity V in an undercooled pure melt. In the PFM with a finite interface width 2ξ , the temperature profile $T(x)$ around the interfacial region changes smoothly as the thick curve shown in Fig. 1. If the condition $\xi \ll D/V$ (so called thin interface limit) is satisfied, the temperature profiles at the regions $\xi \leq |x| \ll D/V$ must be linear, where D is the thermal diffusivity assumed to be same in both phases. The intersection temperature (T^*) of two dotted lines extrapolating the straight profiles at $\xi \leq |x| \ll D/V$ can be taken as the interface temperature corresponding to that in sharp interface limit. The driving force of the interface

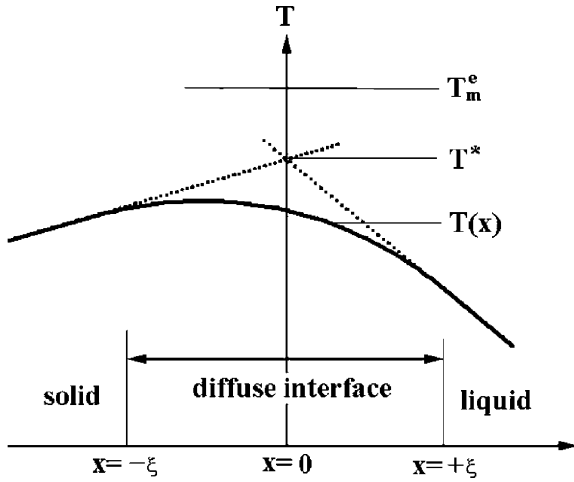


Fig. 1. A schematic temperature profile $T(x)$ (thick line) across the interface in phase-field modeling of solidification in undercooled pure melt, where 2ξ is the interface width and T_m^e is the equilibrium melting temperature. Note that the temperature profiles are linear at the regions $\xi \leq |x| \ll D/V$. Dotted lines are the extrapolations of the linear parts.

motion thus is taken as $T_m^e - T^*$, which is same as that in the sharp interface. Thus the motion of sharp interface with $2\xi \rightarrow 0$ can be described by the PFM with a finite interface width, which greatly enhances the computational efficiency by using a large mesh size in computation. With this thin interface model, Karma and Rappel [13] could compute quantitatively the growth of an isolated dendrite in a pure undercooled melt and extend the computation to 3D case.

Based on the similar role of the chemical potential f_c in alloys as the temperature in pure material, the thin interface analysis for alloy PFM has been performed by us [10] for plane front interface and more recently by Karma [31] for curved interface. Both approaches rely on the assumption $D_S \ll D_L$ which is valid in most alloys, where D_S and D_L are diffusivities in solid and liquid phases, respectively. Here we describe in detail the thin interface analysis for the present eutectic PFM. Apart from our previous approach [10] using the chemical potential, we use the composition field directly.

We consider a plane front interface between solid ($x < 0$; $\phi \equiv \phi_1 = 1$) and liquid ($x > 0$; $\phi = 0$)

phases. When the driving force of solidification is given by Eq. (2.79), the phase field and concentration field at an instantaneous 1D steady state are governed by

$$-\frac{V}{M_{31}} \frac{d\phi}{dx} = \varepsilon_{31}^2 \frac{d^2\phi}{dx^2} - \omega_{31} g'(\phi) + \frac{RT(1-k_1)}{v_m} [c_{31}^e - c_3] p'(\phi), \quad (2.80)$$

$$-V \frac{dc}{dx} = \frac{d}{dx} D [1 - (1-k_1)h(\phi)] \frac{dc_3}{dx}, \quad (2.81)$$

where the primes on the functions g and p denote the derivatives by ϕ , and V is the interface velocity, $g(\phi)$ is a double well potential with the minima at $\phi = 1$ and 0 , $p(\phi)$ is an odd function centered at $\phi = 0.5$ with $p(1) = 1$ and $p(0) = 0$, and $h(\phi)$ also is an odd function centered at $\phi = 0.5$ with $h(1) = 1$ and $h(0) = 0$. We introduced the functions g , p and h to give a general form of thin interface limit condition because various different forms for those functions have been used in literatures, even though $g(\phi) = \phi(1-\phi)$ and $p(\phi) = h(\phi) = \phi$ were adopted in this eutectic PFM. The average composition c , Eq. (2.7), of the mixture at a given point is given by

$$c = c_1 h(\phi) + c_3 [1 - h(\phi)] = c_3 [1 - (1-k_1)h(\phi)]. \quad (2.82)$$

When D_S is very small compared with D_L , the composition in solid is uniform at a steady state. The steady state composition profiles $c(x)$, $c_1(x)$ and $c_3(x)$ across the plane front interface between solid ($\phi = 1$) and liquid ($\phi = 0$) phases are shown in Fig. 2. In this figure, c_{31}^e is the composition of liquid in equilibrium with α phase at temperature T , c_1^* is the uniform solid composition and the coexisting liquid composition is $c_3^* = c_1^*/k_1$. To be precise we should note followings; (i) both the composition profiles $c_1(x)$ for solid and $c_3(x)$ for liquid are defined in the whole space of the system because every point in the system is assumed to consist of a mixture of solid and liquid phases, (ii) the physically real composition is represented by the average composition $c(x)$ of the mixture, given by Eq. (2.82), (iii) the ratio $c_1(x)/c_3(x)$ is constant at the whole space of the system and given by the

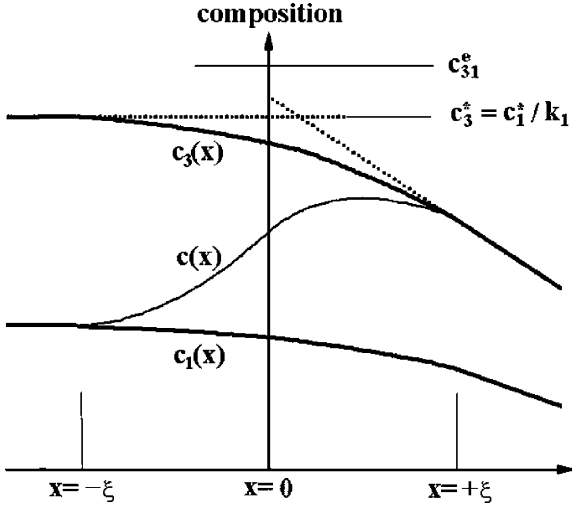


Fig. 2. A schematic diagram of steady state composition profiles $c(x)$, $c_1(x)$ and $c_3(x)$ across a plane front interface between solid ($\phi = 1$) and liquid ($\phi = 0$) phases. Note that $c_1(x)$ for solid and $c_3(x)$ for liquid is defined in the whole space of the system and the physically real composition $c(x)$ is represented by a thin curve which is the average composition given by Eq. (2.82). c_{31}^e is the composition of liquid in equilibrium with α phase at a given temperature and c_1^* is the solid composition at steady state.

equilibrium partition coefficient k_1 according to Eq. (2.76), which is a dilute solution approximation of the equal chemical potential condition (2.5), (iv) The intersection point of the two extrapolated straight lines does not coincide with the origin of the x axis, defined as the position of $\phi = 0.5$, except for the symmetric case of $D_S = D_L$ and $k_1 = 1$ as shown in Appendix B. The deviation of the intersection point from $x = 0$ is related with the jump in chemical potential, which was described in Refs. [30,31].

The supersaturation $c_{31}^e - c_3$ in the bracket in Eq. (2.80) corresponds to the thermodynamic driving force for solidification. Therefore if we set the driving force of the sharp interface motion as $c_{31}^e - c_3^*$, where c_3^* is the intersection point of two straight lines dotted in Fig. 2, Eqs. (2.80) and (2.81) describe the motion of the sharp interface with $2\xi \rightarrow 0$. The analysis can be done as follows: At first, integrating twice Eq. (2.81) under the conditions $dc_3/dx \rightarrow 0$ and $c(x) \rightarrow c_1^* = k_1 c_3^*$ at

$x \rightarrow -\xi$ gives

$$c_3(x) = c_3^* - V \int_{-\xi}^x \frac{c(x) - k_1 c_3^*}{D[1 - (1 - k_1)h(\phi)]} dx. \quad (2.83)$$

The integral in this equation scales as $\sim \xi V / \tilde{D}_i$, where \tilde{D}_i is the average diffusivity in the interfacial region. At the thin interface limit $V\xi / \tilde{D}_i \rightarrow 0$, the integrand can be approximated as that at the equilibrium state with $V = 0$. We then find

$$\begin{aligned} c_3(x) &= c_3^* - V \int_1^\phi \frac{c_0(x) - k_1 c_{31}^e}{D[1 - (1 - k_1)h(\phi_0)]} \frac{dx}{d\phi_0} d\phi_0 \\ &= c_3^* + V(1 - k_1) c_{31}^e \frac{\varepsilon_{13}}{\sqrt{2w_{13}}} \\ &\quad \int_1^\phi \frac{1 - h(\phi_0)}{D[1 - (1 - k_1)h(\phi_0)]} \frac{d\phi_0}{\sqrt{g(\phi_0)}}, \end{aligned} \quad (2.84)$$

where $c_0(x)$ and $\phi_0(x)$ are the composition and phase-field profiles at equilibrium, respectively, which are given by

$$c_0(x) = [1 - (1 - k_1)h(\phi_0)]c_{31}^e, \quad (2.85)$$

$$\frac{d\phi_0}{dx} = -\frac{\sqrt{2\omega_{13}}}{\varepsilon_{13}} \sqrt{g(\phi_0)}. \quad (2.86)$$

After putting Eq. (2.84) into the phase-field equation (2.80), integrating the equation after multiplying $d\phi/dx$ on both sides leads to

$$\begin{aligned} T_E - T &= m_1(c_E - c_3^*) - V \left[\frac{v_m}{M_{13}RT} \frac{m_1}{1 - k_1} \frac{\sigma_{13}}{\varepsilon_{13}^2} \right. \\ &\quad \left. - \frac{m_1 \varepsilon_{13}}{\sqrt{2\omega_{13}}} (1 - k_1) c_{31}^e \zeta_{13} \right], \end{aligned} \quad (2.87)$$

where the constant ζ_{13} is given by

$$\zeta_{13} = \int_0^1 \frac{p(\phi_0)[1 - h(\phi_0)]}{D[1 - (1 - k_1)h(\phi_0)]} \frac{d\phi_0}{\sqrt{g(\phi_0)}}. \quad (2.88)$$

In the classical sharp interface model, the interface undercooling below the eutectic temperature T_E is given by the sum of constitutional undercooling and kinetic undercooling when the curvature undercooling is ignored as in this present analysis;

$$T_E - T = m_1(c_E - c_3^*) + \beta_{13}V. \quad (2.89)$$

This equation can be matched with Eq. (2.87) if we put the kinetic coefficient β_{13} as

$$\beta_{13} = -\frac{v_m}{M_{13}RT} \frac{m_1}{1-k_1} \frac{\sigma_{13}}{\varepsilon_{13}^2} + \frac{m_1(1-k_1)\varepsilon_{13}}{\sqrt{2\omega_{13}}} c_{31}^e \zeta_{13}. \quad (2.90)$$

The second term in the right hand side of this relationship corresponds to the correction in the kinetic coefficient due to the finite interface width effect at the thin interface limit. For β - L interface, a similar relationship can be derived between the interface kinetic coefficient β_{23} and phase-field mobility M_{23} .

It should be mentioned that above simple analysis was performed for 1D plane front interface. As shown by Almgren [30], the rigorous analysis for a curved interface revealed the anomalous effects such as chemical potential jump, interface stretching and surface diffusion at the interface. Present eutectic PFM are free from the surface stretching effect because we adopt $h(\phi) = \phi$, but not from the chemical potential jump and surface diffusion effects at the interface. Under our computational conditions for CBr_4 – C_2Cl_6 organic alloys, however, the chemical potential jump appears to be negligibly small, as shown in Appendix B. Also we note that in eutectic solidification the surface diffusion effect driven by the curvature gradient is relatively smaller than in the primary dendritic solidification with a large curvature gradient at the tip.

3. Computation methods

The lamella eutectic growth and instability of the growth front in CBr_4 – C_2Cl_6 organic alloys have been experimentally studied by Akamatsu et al. [25–28]. The present PFM of eutectic solidification was applied to simulate their experiments, due to following two reasons: First their experiments were performed in 2D geometry with thin specimens. Various instability patterns during the coupled eutectic growth appeared due to the prevention of 3D lamella branching. Second all the physical parameters necessary for the phase-field computations were carefully measured with a

reasonable accuracy [26]. In this section we describe the determination of the phase-field parameters and numerical methods taken to simulate the experiments under the same conditions.

We use the physical parameters measured around the eutectic temperature [26]; diffusivity in liquid and solid are $D_L = 5 \times 10^{-10} \text{ m}^2/\text{s}$ and $D_S = 5 \times 10^{-14} \text{ m}^2/\text{s}$, respectively, eutectic temperature is $T_E = 357.6 \text{ K}$, the eutectic composition is $c_E = 0.118$ mol fraction, the equilibrium liquidus slopes of α phase and β phase are $m_1 = -81 \text{ K}$ and $m_2 = 165 \text{ K}$, respectively, the partition coefficients in α and β phases to the liquid phase L are $k_1 = 0.75$ and $k_2 = 1.6$, respectively, α - L , β - L and α - β interface energies are $\sigma_{31} = 6.6 \times 10^{-3}$, $\sigma_{32} = 5.8 \times 10^{-3}$ and $\sigma_{12} = 11.5 \times 10^{-3} \text{ J/m}^2$, respectively, and the molar volume is $v_m = 1.12 \times 10^{-4} \text{ m}^3/\text{mol}$. The kinetics coefficients were taken to be $\beta_{13} = \beta_{23} = 0$ to use the vanishing interface kinetics condition for α - L and β - L interfaces. In simulating the pattern formation of directional eutectic solidification all the interface energies were assumed to be isotropic, following the suggestion in Ref. [28]. Also we test the maintenance of mechanical equilibrium at the triple junction under a thermal gradient for both isotropic and anisotropic PFMs. The phase-field computations for lamella growth were performed at two different bulk compositions of C_2Cl_6 . One is the eutectic alloy $c_0 = c_E$ having an β phase volume fraction of 0.29 and the other is hypereutectic alloy $c_0 = (k_1 + k_2)c_E/2$ having the same α and β volume fraction. The hypereutectic alloy was chosen because of the extensive studies [25–28] on the tilt and/or oscillatory instabilities in the coupled growth of the lamellar patterns. The thermal gradient G was fixed to be $0.8 \times 10^4 \text{ K/m}$ as in the experiments. We computed the growth pattern as a function of lamellar spacing at a fixed pulling velocity $V = 2 \text{ }\mu\text{m/s}$, even though the experiments were performed at various pulling velocities ($1 \sim 4 \text{ }\mu\text{m/s}$) with predetermined lamellar spacings ($10 \sim 100 \text{ }\mu\text{m}$).

The phase-field parameters ω_{ij} and ε_{ij} were obtained from Eqs. (2.35) and (2.36);

$$\omega_{ij} = 2 \frac{\sigma_{ij}}{\xi}, \quad (3.1)$$

$$\varepsilon_{ij} = \frac{4}{\pi} \sqrt{\xi \sigma_{ij}}. \quad (3.2)$$

From the preliminary computations, we found that resolving the interfacial region into seven grids yielded a good compromise between minimizing the grid anisotropy and maximizing the computational efficiency. We fixed the interface width $2\xi = 7\Delta x$ in all computations. The phase-field mobilities (M_{i3} for $i = 1, 2$) were determined at the vanishing kinetics coefficient condition ($\beta_{i3} = 0$ for $i = 1, 2$) in Eq. (2.90);

$$M_{i3} = \frac{v_m}{RT} \frac{\sigma_{i3}}{(1 - k_i)^2} \frac{\sqrt{2\omega_{i3}}}{c_{3i}^e \varepsilon_{i3}^3 \xi_{i3}}. \quad (3.3)$$

The constant ξ_{i3} is given by

$$\xi_{i3} = \frac{1}{D_L} \int_0^1 \frac{\sqrt{\phi(1-\phi)}}{[1 - (1 - k_i)\phi]} d\phi, \quad (3.4)$$

where we used $g(\phi) = \phi(1 - \phi)$ and $p(\phi) = h(\phi) = \phi$ in Eq. (2.88) to be in accordance with Eqs. (2.19) and (2.24). Two points should be mentioned in using Eqs. (3.3) and (3.4); First they were derived under the condition of $D_S \ll D_L$. Therefore those relationship can not be hold for $\alpha - \beta$ interface because the solid state phase transformation cannot take place here. We therefore simply assumed $M_{12} = (M_{13} + M_{23})/2$ in present computations. Secondly, Eq. (3.4) assumes the diffusivity in the interfacial region is constant and same as the liquid diffusivity, which was to minimize the solute trapping effect at the interfacial region.

The mesh size $\Delta x = \Delta y$ on the uniform square grid system was selected by considering the experimental results; during the lamella growth in $\text{CBr}_4\text{--C}_2\text{Cl}_6$ alloy, the minimum lamellar spacing λ^{\min} at $V = 2 \mu\text{m/s}$ was close to $10 \mu\text{m}$, fairly independent of the composition [28]. For resolving the radius $R_i (\simeq \lambda^{\min}/2)$ of the solid–liquid interface curvature, the interface width $2\xi (= 7\Delta x)$ must be sufficiently smaller than R_i . From the preliminary computations on an isolated circular solid particle in a liquid matrix, we found that if $R_i \geq 4\xi$ then the PFM computation recovers the Gibbs–Thomson effect within 5% error. Based on the result, we took $\Delta x = 0.2 \mu\text{m}$ for all computations. With this choice, we see that

$R_i \simeq \lambda^{\min}/2 = 25\Delta x \simeq 7\xi$ and so the Gibbs–Thomson effect in phase-field computations can be recovered with a good accuracy even for the minimum lamellar spacing.

Three different system sizes were adopted: The first system with $I_m \times J_m = 130 \times 50$ meshes was used for the test of the force balance at the triple junction between a grain boundary and two solid/liquid interface. The second system with $I_m \times 4,000$ meshes was used for eutectic alloy solidification. The number I_m (meshes perpendicular to the thermal gradient direction) was varied in the range of $60 \sim 300$ to include two lamellar spacings, depending on the given initial lamellar spacing. Although it might be better to include the lamellae as many as possible for getting the statistical characteristics of the system, transient time from the initial lamellar pattern to the oscillatory or tilted patterns was too long to show the coherent behavior of all patterns. A few preliminary computations with doubled I_m and four lamellar spacings gave almost identical results as the case of two lamellar spacings. The third system with $I_m \times 20,000$ meshes was used for the coupled lamella growth of the hypereutectic alloy with composition $c_0 = (k_1 + k_2)c_E/2$. In the coupled growth of the off-eutectic alloy there exists an additional long-range diffusion field as well as the exchange diffusion field near the front interface. Though the diffusion layer thickness of this long-range field is in the order of $D_L/V = 250 \mu\text{m} = 1,250\Delta x$, we used $J_m = 20,000$ along the growth direction to keep the long tail (about $10,000\Delta x$) of the field far away from the end wall of the system. To enhance the computational efficiency in this large grid system, at every time step we checked the maximum composition difference Δc_{\max} in I direction for every J 's, starting from $J = 1$. If Δc_{\max} at $J = J^*$ became less than $10^{-4}\%$ for the first time, then 1D diffusion equation was solved in the region of $J > J^*$. Because the distance between J^* and the front interface appeared to be less than a few hundreds meshes, above simple treatment was very efficient and the CPU time (several days with a Pentium III CPU) was comparable to that for the eutectic alloy.

We solved numerically the diffusion equation (2.24) and the isotropic phase-field equation (2.18)

for lamella growth or the anisotropic phase-field equation (2.56) to test the maintenance of mechanical equilibrium at the triple junction, both under the same thermal gradient. In all computations Eqs. (2.77) and (2.78) were used for the thermodynamic terms in the phase-field equation. The equations were discretized by the standard explicit finite difference scheme.

One should be careful of numerical treatment of the step function $s_{ij} = s_i s_j$. If we use s_i following the definition, $s_i(x, t) = 1$ if $\phi_i > 0$ and $s_i(x, t) = 0$ otherwise, there can not be any propagation of the phase field in the region initialized by $s_{ij} = 0$ (that is, $\phi_i = 0$ or $\phi_j = 0$). This problem was circumvented by simply modifying the definition as $s_i(x, t) = 1$ if the sum of ϕ_i 's on the four nearest neighbor grids is between δ and $4 - \delta$, $s_i(x, t) = 0$ otherwise, where δ is a small positive. With this definition, the phase field could propagate because the grids neighboring to the interfacial region between i and j phases can become $s_i = 1$ or $s_j = 1$. Even though it looks reasonable to take $\delta = 0$, it made the interface width unstable, due to the definite interface region originating from the parabolic double-well potential used in present study. Through a systematic test on the δ value effect on eutectic lamellar pattern, in the range $0.01 < \delta < 0.05$, we found not only stable interfaces but also good reproducibility in lamella morphology in quantitative details. Thus we used $\delta = 0.02$ in all the computations following.

As initial boundary conditions, we put alternating α and β phases with equilibrium volume fractions and assumed the temperature of the planar solid–liquid interface to be T_E . A periodic boundary condition was imposed on the system boundaries parallel to the thermal gradient direction, while adiabatic condition on the other two boundaries. Most computations were proceeded until the solidification front reaches $1000 \Delta x$. The transition time from the initial regular lamellar pattern to tilt or oscillatory pattern was slightly influenced by the noise, if it occurs within the computation time. Thus a small random white noise (0.2%) in concentration field was imposed at the interfacial region, conserving the total mass.

4. Computation results

4.1. Force balance at triple junction

The force balance at a triple junction between solid and liquid phases and the Gibbs–Thomson effect play important roles in the evolution of interface patterns during eutectic solidification. For quantitative computation of the patterns, therefore, it is prerequisite to test whether the Gibbs–Thomson effect and the force balance at the triple junction are recovered correctly in the present eutectic PFM. We compute the equilibrium grain boundary groove shape under a constant thermal gradient, because the shape is governed by both the Gibbs–Thomson undercooling and the groove angle determined by the force balance condition.

Consider an equilibrium between two α grains and liquid under a constant thermal gradient, shown in Fig. 3. θ was defined as the angle between the direction normal to the solid–liquid interface and the x axis. The angle θ^* at the triple junction of the groove is determined by the force balance condition

$$\sigma_g - 2 \frac{d\sigma_{13}}{d\theta} \sin \theta - 2\sigma_{13} \cos \theta = 0, \quad (4.1)$$

where the second term is the torque force originating from the anisotropy of interface energy σ_{13} , and σ_g is the grain boundary energy assumed to be isotropic. We assume the four fold anisotropy of the form

$$\sigma_{13} = \sigma_{13}^0 [1 + \delta_\sigma \cos 4(\theta - \theta_0)], \quad (4.2)$$

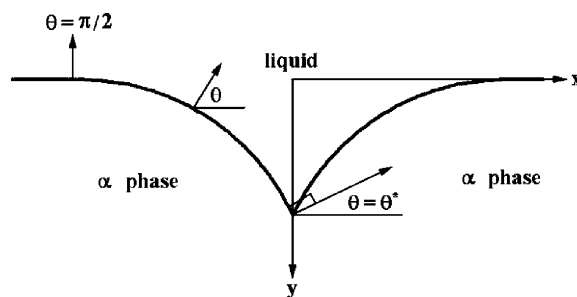


Fig. 3. An equilibrium between two α grains and liquid, where θ is the angle between the x axis and the direction normal to the solid–liquid interface. The angle θ^* at the triple junction of the groove is determined by the force balance condition.

where σ_{13}^0 is the average interface energy and θ_0 is the orientation with the maximum interface energy. For given σ_g and σ_{13}^0 , the angle θ^* can be found from the numerical solution of Eq. (4.1). The equilibrium groove shape under a constant thermal gradient G can be easily found from the balance between the thermal undercooling arising from the imposed gradient and the curvature undercooling due to the Gibbs–Thomson effect. Under the boundary conditions $\theta = \theta^*$ at $x = 0$ and $\theta = \pi/2$ at $y = 0$, the solution is given by a parametric form Ref. [32]

$$x = \frac{1}{aG} \int_{\theta^*}^{\theta} \frac{\sin \theta}{y} \left(\sigma_{13} + \frac{d^2 \sigma_{13}}{d\theta^2} \right) d\theta, \quad (4.3)$$

$$y^2 = \frac{2}{aG} \left[\sigma_{13, \theta=\pi/2} - \sigma_{13} \sin \theta - \frac{d\sigma_{13}}{d\theta} \cos \theta \right], \quad (4.4)$$

where the constant a for an alloy is

$$a = \frac{RT_E}{v_m} \frac{k_1 - 1}{m_1}. \quad (4.5)$$

By using the van't Hoff relation, this constant may be replaced by more familiar form, $a \approx \Delta H / T_m^e$, where ΔH is the heat of fusion. The equilibrium groove shape is obtained by numerical integration of Eqs. (4.3) and (4.4). All the parameters are the same as those given in previous section, except for the diffusivity and the grain boundary energy σ_g . For fast convergence to the equilibrium state, the liquid diffusivity D_L was assumed to all space including the solid and interface region. Note that the diffusivity do not affect the final equilibrium state where the diffusional flux completely disappears at the whole space of the system. σ_g was varied to test the groove angle effect.

Fig. 4 shows the groove shapes computed using the isotropic PFM (white regions) for (a) $\sigma_g = \sigma_{13}^0$, (b) $\sigma_g = 1.5\sigma_{13}^0$ and (c) $\sigma_g = 1.95\sigma_{13}^0$. Also the exact solutions (solid curves) obtained from Eqs. (4.3) and (4.4) with $\delta_\sigma = 0$ were included for comparison in Fig. 4. In these figures the grid points in the mesh system were inscribed as small dots, but the region where the phase-field values are between 0.1 and 0.9 was remained blank. Even though the angles at the triple junction can not be quantitatively compared because of the interface diffuseness in PFM computations, one can see that the computed groove shapes are very close to the exact

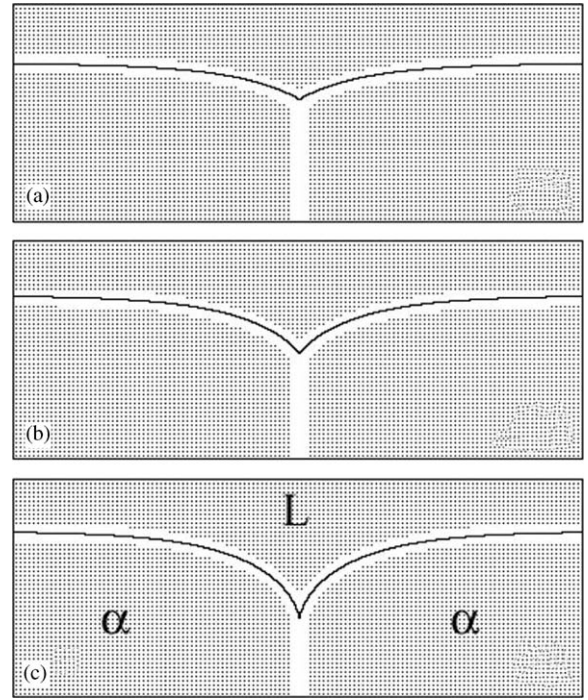


Fig. 4. Equilibrium groove shapes computed with the isotropic PFM (white regions) and the exact solutions (solid curves), for (a) $\sigma_g = \sigma_{13}^0$, (b) $\sigma_g = 1.5\sigma_{13}^0$ and (c) $\sigma_g = 1.95\sigma_{13}^0$. The grid points in the mesh system were inscribed as small dots, but the region where the phase-field values are between 0.1 and 0.9 was remained blank.

solutions, independent of the relative interface energies. At the condition $\sigma_g > 2\sigma_{13}$, the complete wetting of the grain boundary by liquid phase could be observed. Fig. 5 shows the similar results computed using the anisotropic PFM with $\delta_\sigma = 0.05$ and $\sigma_g = \sigma_{31}^0$ for (a) $\theta_0 = \pi/4$ and (b) $\theta_0 = 0$. The solid curve on the left half space of each figure corresponds to the exact solution. In order to show the anisotropy effect more clearly, the isotropic exact solution with $\delta_\sigma = 0$ also is shown by a solid curve on the right half space. We see that the computed groove shapes are very close to the exact solutions. The opposite deviation of the anisotropic interfaces with $\theta_0 = 0$ and with $\theta_0 = \pi/4$, from the isotropic case can be easily understood: When $\theta_0 = \pi/4$, the interface energy given by Eq. (4.2) becomes minimum at $\theta = 0$, corresponding to the planes parallel to the x axis or y axis. Thus the solid–liquid interface tends to deflect

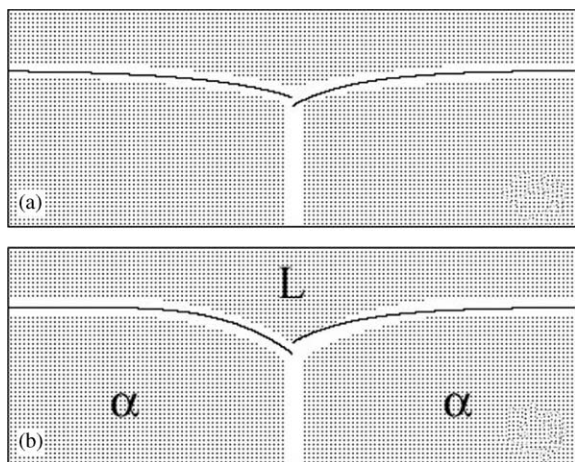


Fig. 5. Equilibrium groove shapes computed with the anisotropic PFM (white regions) with $\sigma_g = \sigma_{31}^0$, $\delta_\sigma = 0.05$ and (a) $\theta_0 = \pi/4$ and (b) $\theta_0 = 0$. The solid curves on the left half space and right half space of each figure are the exact solutions with anisotropy $\delta_\sigma = 0.05$ and without the anisotropy ($\delta_\sigma = 0$), respectively.

toward the plane parallel to the x axis, as in (a) of Fig. 5. When $\theta_0 = 0$, on the other hand, the solid–liquid interface tends to deflect toward the orientation with $\theta = \pi/4$, where the interface energy is minimum. All these excellent agreement of the computed groove shapes with the exact solutions support that the force balance at triple junction and the Gibbs–Thomson effect are not only satisfied with good accuracy in present PFM, but also anisotropic phase-field equations (2.56) and (2.57) operates in a right way.

4.2. Lamella solidification

Since a rich dynamical behavior in eutectic growth was demonstrated by using MonteCarlo simulations [33], experimental and theoretical studies on the oscillatory and tilt instabilities in the lamellar pattern have been performed [25–28,34–37] in details for eutectic and off-eutectic alloys. The most extensive studies to date seem to be the experiments by Ginibre et al [28] for organic alloys ($\text{CBr}_4\text{--C}_2\text{Cl}_6$) and numerical computations by Karma and Sarkissian [37] using a Green function method. Especially Ginibre et al. [28] showed that the numerical computations [37] with isotropic interface energy were in good agreement

with their observations. In this section we show computation results of the isotropic eutectic PFM with main focus on the oscillatory and tilt instabilities in the eutectic and hypereutectic alloys. The main objective of the computations is the test of the our eutectic PFM by comparing directly the computational results with experimental results. Therefore it is beyond the scope of this study to clarify the existence conditions or mechanisms of the instabilities.

Before presenting the computation results, it is worthwhile to note followings; The width of computation domain is twice of the lamellar spacing, but each computed pattern was multiplied in all figures to show clearly the overall image of the pattern. We use the volume fraction f_β of β phase instead of alloy composition. Two different compositions were considered in the computations, the eutectic composition with $f_\beta = 0.29$ and hypereutectic composition with $f_\beta = 0.5$. Following Refs. [28,37], we introduce a dimensionless lamellar spacing Λ defined as the ratio $\lambda/\lambda_{\text{JH}}$, where λ is the lamellar spacing and λ_{JH} is the minimum-undercooling spacing in the Jackson and Hunt's eutectic theory [38]. With the isotherm velocity $V = 2 \mu\text{m/s}$ fixed in all computations, we find $\lambda_{\text{JH}} = 10.13 \mu\text{m}$ for $f_\beta = 0.29$ and $\lambda_{\text{JH}} = 9.79 \mu\text{m}$ for $f_\beta = 0.5$ from the equation given in Ref. [28]. If the alloy composition is given, the transition threshold between the patterns is governed by the dimensionless lamellar spacing Λ [28,37]. For quantitative comparison, we compare the transition thresholds in phase-field computations with those observed in experiments. For denoting each characteristic pattern, we will follow the notations by Ginibre et al. [28].

For the eutectic alloy, we computed the interface undercooling as a function of the lamellar spacing, which was shown in Fig. 6. The curve shows the relationship obtained from the Jackson–Hunt's theory and the filled circles exhibit the results of the PFM computations. The interface temperature was assumed to be the average temperature over the entire interface position corresponding to $\phi_3 = 0.5$. Below a critical spacing, the interface undercooling could not be estimated due to the occurrence of lamella termination phenomenon. The critical spacing λ_c

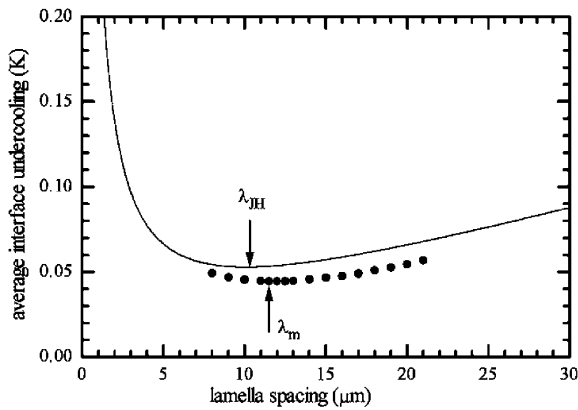


Fig. 6. Variation of interface undercooling as a function of the lamellar spacing for the eutectic alloy. The curve is the relationship from the Jackson–Hunt's theory and the filled circles are the results from PFM computations.

for the termination was slightly dependent on the number of the lamella pairs in the computation system. For the system with two lamella pairs which were shown in Fig. 6, λ_c appeared to be close to 8 μm . For the system with eight lamella pairs, λ_c was 8.7 μm . These critical spacings correspond to $\lambda_c = (0.70 \sim 0.76) \lambda_m$, where λ_m is the spacing corresponding to the minimum interface undercooling as marked in the figure. The similar behavior has been experimentally observed for $\text{CBr}_4 - \text{C}_2\text{Cl}_6$ organic alloys [39]. The computed spacing at the minimum undercooling is larger than λ_{JH} by about 10%. The computed interface undercoolings are lower than those from Jackson–Hunt theory by about 20%. The anomalous interface diffusion in our PFM may be responsible in part for these differences between computations and theory.

With increasing the lamellar spacing over λ_m , the regular lamella eutectic structure with straight $\alpha - \beta$ boundaries parallel to the thermal gradient direction appeared to be stable up to $\Lambda \approx 2.1$. However an oscillatory pattern with a wavelength of one lamellar spacing and with periodic modulations in widths of α and β phases appeared at $\Lambda = 2.3$. This pattern ($1\lambda O$ pattern in Ref. [28]) was observed also at $\Lambda = 2.5$ as shown in Fig. 7, where the minor phase is β . With increasing Λ above 2.5, transition of the pattern takes place; at the initial stage of growth the $1\lambda O$ -like pattern appeared first

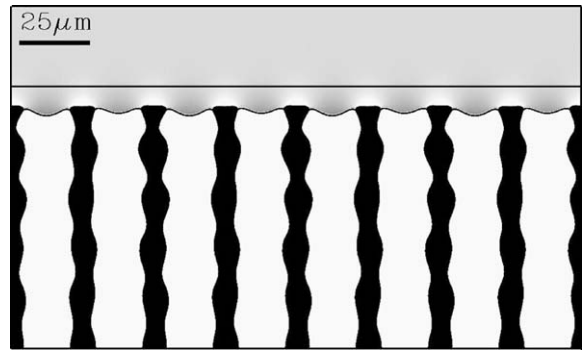


Fig. 7. $1\lambda O$ pattern at $\Lambda = 2.5$ from the PFM computation for eutectic alloy, where the minor phase is β .

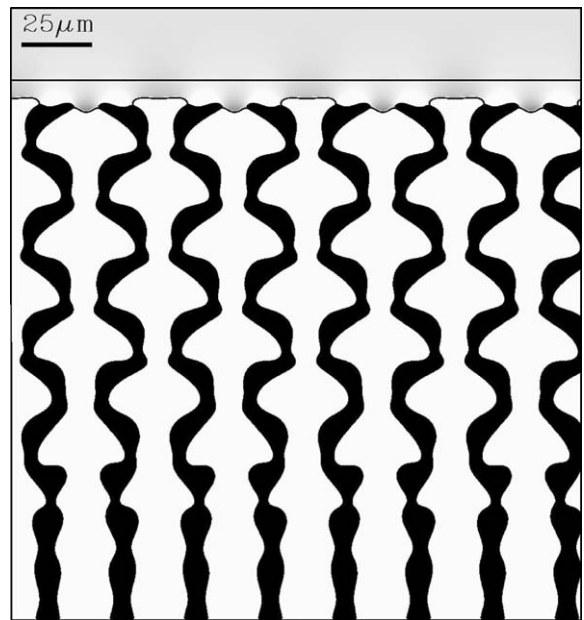


Fig. 8. A transient of $1\lambda O$ pattern to $2\lambda O$ pattern obtained at $\Lambda = 2.7$ from the PFM computation for eutectic alloy.

but after a transient period the pattern transformed into another oscillatory pattern with a wavelength of twice the lamellar spacing. The pattern is characterized by the wavy β phase and modulated α phase, which was called $2\lambda O$ pattern in [28]. The transient period of $1\lambda O$ pattern to $2\lambda O$ pattern decreased with increasing Λ further. The $2\lambda O$ pattern persisted even at $\Lambda = 3$, the maximum lamellar spacing of our computation. Fig. 8 is a computation result obtained at $\Lambda = 2.7$, showing a

Table 1

Comparison of computations and experiments on the characteristic scales of the oscillatory patterns of the eutectic alloy.

pattern	f_β	V ($\mu\text{m/s}$)	λ (μm)	Λ	$\lambda^2 V$ ($\mu\text{m}^3/\text{s}$)	λ_O/λ	Ref.
$1\lambda O$	0.28	0.5	50	2.5	1250	0.62	Fig. 13 in [28]
$1\lambda O$	0.29	2.0	25	2.5	1250	0.62	This study
$1\lambda O - 2\lambda O$	0.28	0.46	60	2.7	1660	—	Fig. 14 in [28]
$2\lambda O$	0.29	2.0	27	2.7	1460	—	this study

typical transition from $1\lambda O$ to $2\lambda O$ pattern. These results on the stability domain of each pattern and sequence of pattern change in the eutectic composition are in close resemblance with the experimental results; stable regular lamellar pattern at $\Lambda < 2.2$, $1\lambda O$ pattern at $2.2 < \Lambda < 2.5$ and so called $1\lambda O - 2\lambda O$ pattern at $\Lambda > 2.5$ [28]. The last pattern ($1\lambda O - 2\lambda O$) in experiments appears to be similar to the transient pattern between $1\lambda O$ and $2\lambda O$ in Fig. 8. But it is not clear why such $1\lambda O - 2\lambda O$ pattern could not persist in our computations. The characteristic scales in our computations can be compared further in details with the figures shown in Ginibre et al. Ref. [28]. Table 1 shows the comparison of the values $\lambda^2 V$ and λ_O/λ , where λ_O is the wavelength of the modulation in α and β phases. Among the several computational results giving a same pattern, we took one showing the closest Λ values to the figures in Ref. [28]. Experiments Ref. [28] showed that the lamellar spacing λ follows the scaling law $\lambda \sim V^{-1/2}$ for each patterns, except a rather large statistical deviation in the $2\lambda O$ pattern. Thus The $\lambda^2 V$ values for most patterns remain independent of V . Table 1 shows that our computation results of $\lambda^2 V$ are very close to those from experiments. Also the relative wavelength of the modulation to the lamellar spacing in the $1\lambda O$ pattern is in good agreement with the experiments. These agreements with experiments imply that the present eutectic PFM is correctly operating to make quantitative sense in computations at the eutectic composition.

In the hypereutectic composition corresponding to $f_\beta = 0.5$, we computed the solidification patterns in the range of $10 \mu\text{m} \leq \lambda \leq 30 \mu\text{m}$ ($1.0 \leq \Lambda \leq 3.0$) with $1 \mu\text{m}$ interval, as in eutectic composition. The regular lamellar structure appeared stable at lamellar spacing $\Lambda \leq 1.2$. With increasing the lamellar spacing, however, the

regular lamellar pattern became unstable and then four different patterns formed depending on Λ values: $2\lambda O$ pattern at $1.3 \leq \Lambda \leq 1.5$, characterized by the wavy α phase and modulated β phase; $T - 2\lambda O$ pattern at $1.6 \leq \Lambda \leq 1.8$, corresponding to the tilted version of $2\lambda O$ pattern; T pattern at $\Lambda = 1.9$, the tilted lamellar pattern without any oscillatory instability; and $T - 1\lambda O$ pattern at $\Lambda \geq 2.0$, characterized by the 1λ periodicity in the solid–liquid interface shape and oscillation in lamella width of both α and β phases. The typical patterns at various Λ values are shown in Fig. 9, for (a) $2\lambda O$ at $\Lambda = 1.3$, (b) $T - 2\lambda O$ at $\Lambda = 1.6$, (c) T at $\Lambda = 1.9$ and (d) $T - 1\lambda O$ at $\Lambda = 2.3$ patterns. In this figure, the white region is α phase. The tilt direction could be reversed by slight change in the initial conditions or the noise generation sequence. Each pattern can be characterized by the existence domain in Λ , the scales $\lambda^2 V$, λ_O/λ and the tilting angle. The results from computations on the first three were compared with those from the experiments, which is shown in Table 2. Here we took the computation results obtained at the closest Λ values to the figures shown in [28] for the hypereutectic compositions, within the range showing the same kind of the pattern. From this table, we note followings: Firstly, the sequence of pattern change with lamellar spacing is same as the experimental observation. Secondly, the existence domain (Λ ranges) of each pattern is in fair agreement with experiment. Even though the differences between computations and experiments on the Λ domains of $2\lambda O$ and T patterns look rather large in Table 2, they are within the range of the scattered data in Fig. 17 in Ref. [28]. Also the $\lambda^2 V$ values computed for each pattern are very close to the experimental values. The most significant difference between the computations and experiments appears in $\lambda^2 V$ and λ_O/λ values of the

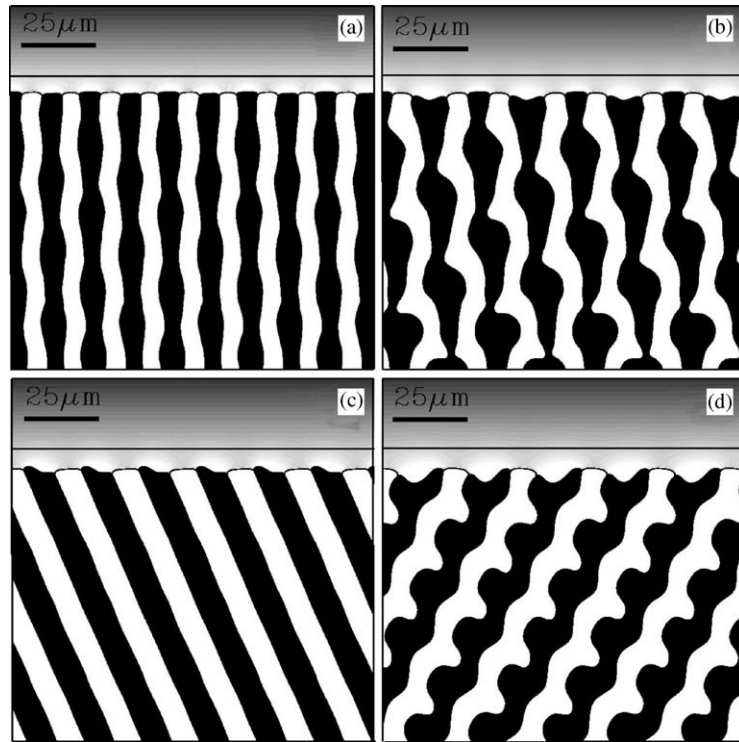


Fig. 9. Typical patterns obtained at various Λ values from PFM computations for the hypereutectic alloy ($f_\beta = 0.5$); (a) $2\lambda O$ at $\Lambda = 1.3$, (b) $2\lambda O$ at $\Lambda = 1.6$, (c) T at $\Lambda = 1.9$ and (d) $T - 1\lambda O$ at $\Lambda = 2.3$. The white region is α phase.

Table 2

Comparison of computations and experiments on the characteristic scales of the tilt and/or oscillatory patterns

pattern	f_β	V ($\mu\text{m/s}$)	λ (μm)	Λ	$\lambda^2 V$ ($\mu\text{m}^3/\text{s}$)	λ_O/λ	Ref.
$2\lambda O$	0.48	1.52	12	1.1	220	4.4	Fig. 8 in [28]
$2\lambda O$	0.5	2.0	13	1.3	340	1.9	this study
$T - 2\lambda O$	0.44	0.7	27	1.6	500	1.8	Fig. 11 in [28]
$T - 2\lambda O$	0.5	2.0	16	1.6	510	1.9	this study
T	0.45	0.8	29	1.6	670	—	Fig. 4 in [28]
T	0.5	2.0	19	1.9	720	—	this study
$T - 1\lambda O$	0.35	1.55	26	2.4	1050	0.9	Fig. 7 in [28]
$T - 1\lambda O$	0.5	2.0	23	2.3	1060	0.8	this study

$2\lambda O$ pattern. The origin of the difference is not clear, even though it might be due to the anomalous interface diffusion effect. One of the interesting characteristics of each pattern is the tilting angle of the pattern from the thermal gradient direction. In Fig. 10, we compared the tilting angles in computations with the experimentally observed angles [28], where the open symbols are from experiments and the filled ones from the computations. Even though

the data in [28] were obtained from alloys with compositions ranging $0.4 \leq f_\beta \leq 0.47$, the overall trend of the tilting angle variation with Λ is quite similar each other. Especially, the steep change in the tilting angle during the transition from $T - 2\lambda O$ to T pattern can be seen in both the computations and experiments. We can see the Λ domains computed for each pattern also are close to those from experiments.

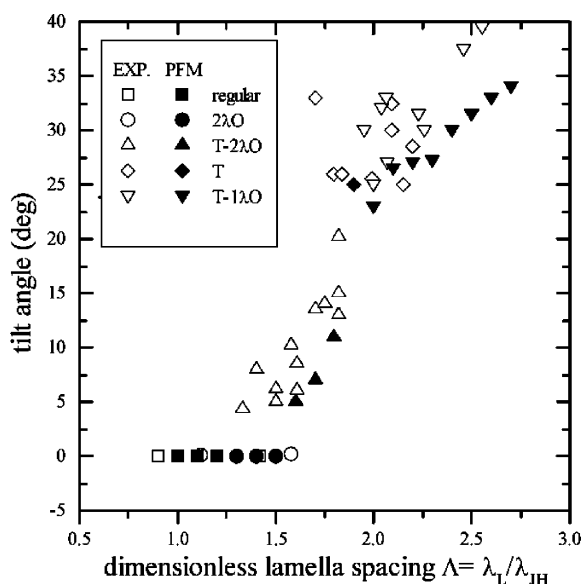


Fig. 10. Tilting angles of each pattern as a function of Λ , where the open symbols are the experimental data [28] observed from alloys with compositions ranging $0.4 \leq f_\beta \leq 0.47$ and the filled ones are the computation results for $f_\beta = 0.5$.

5. Summary

Although several phase-field models have been proposed for eutectic solidification, there has not been a quantitative computation which can be directly compared with experimental results, possibly due to the limitations of each model. In this study we developed a eutectic phase-field model and applied the model to simulate directional eutectic solidification of thin film $\text{CBr}_4\text{--C}_2\text{Cl}_6$ organic alloys under the same experimental conditions without any fitting parameter.

The eutectic phase-field model was derived using the interface field method under the condition that the coexisting phases at a given point have an equal chemical potential difference between solute and solvent. Also anisotropic eutectic phase-field equation accounting for the anisotropies of material's parameters was derived. Thin interface analysis was performed to derive a relationship between the phase-field mobility and interface kinetics coefficient.

The equilibrium interface shapes, computed using the phase-field model, at a triple junction

under a thermal gradient were in good agreement with the exact solutions for both isotropic and anisotropic solid–liquid interface energies, which indicates the maintenance of force equilibrium at triple junction in present eutectic phase-field models.

PFM computations under the real experimental conditions without any fitting parameters reproduces a variety of eutectic lamellar patterns observed in the experiments. Most of the characteristics of the pattern change with lamellar spacing in both eutectic and hypereutectic alloys are in good agreement with experimental observations.

Acknowledgements

S.G. Kim and W.T. Kim thanks for the financial support from Korea Science and Engineering Foundation through a basic research grant program (R01-2002-000-00181-0(2002)).

Appendix A. Extra double-well potential under the equal composition condition

Many phase-field models for alloy solidification assume that any point within the interfacial region is a mixture of solid and liquid phases with an equal composition, in contrast to our approach with an equal chemical potential. Even though the restriction on the interface width under the equal composition condition has been briefly discussed in Refs. [10,24,40], in this appendix we give a detailed explanation of (i) the existence of the extra chemical potential, (ii) an explicit functional form of the potential and (iii) a grid size restriction arising from the potential.

We consider an equilibrium state having a flat boundary between solid S ($\phi_1 = 1$) at $x < 0$ and liquid L ($\phi_3 = 1$) at $x > 0$;

$$\varepsilon^2 \frac{d^2 \phi}{dx^2} - \omega \frac{dg}{d\phi} - f_\phi = 0, \quad (\text{A.1})$$

$$\frac{d}{dx} \frac{D}{f_{cc}} \left(\frac{d}{dx} f_c \right) = 0, \quad (\text{A.2})$$

where we put $\phi \equiv \phi_1 = 1 - \phi_3$, $\varepsilon_{13} = \varepsilon$ and $\omega_{13} = \omega$. The composition of the bulk solid and liquid phases are c_S^e and c_L^e , respectively. If the coexisting phases at a spatial point within the interfacial region were assumed to have an equal composition $c_1(x, t) = c_3(x, t) \equiv c$,

$$(A.3)$$

then the free energy density is given by

$$f(c, \phi) = h(\phi)f^S(c) + [1 - h(\phi)]f^L(c). \quad (A.4)$$

Because the mass flux disappears at the equilibrium state, the solution of Eq. (A.2) is $f_c =$ (constant) over the whole space of the system, that is,

$$f_c = f_c^S = f_c^L \equiv f_c^e. \quad (A.5)$$

This can be written as

$$\frac{df_c}{dx} = f_{cc} \frac{dc}{dx} + f_{c\phi} \frac{d\phi}{dx} = 0, \quad (A.6)$$

that is,

$$\frac{dc}{d\phi} = -\frac{f_{c\phi}}{f_{cc}}. \quad (A.7)$$

Integrating Eq. (A.7) yields the equilibrium composition profile $c(\phi)$ as a function of the phase field.

Now we turn to the phase-field equation (A.1). By using

$$f_\phi = \frac{df}{d\phi} - f_c \frac{dc}{d\phi} = \frac{d}{d\phi} (f - cf_c^e), \quad (A.8)$$

we can modify the Eq. (A.1) as

$$\varepsilon^2 \frac{d^2 \phi}{dx^2} = \frac{d}{d\phi} [\omega g(\phi) + f - cf_c^e]. \quad (A.9)$$

After multiplying $d\phi/dx$ on both sides, we integrate this equation from $-\infty$ to x ;

$$\begin{aligned} \frac{\varepsilon^2}{2} \left(\frac{d\phi}{dx} \right)^2 &= \omega g(\phi) + f(c(\phi), \phi) - f^S(c_S^e) \\ &\quad - [c(\phi) - c_S^e] f_c^e \equiv \omega g(\phi) + G(\phi). \end{aligned} \quad (A.10)$$

The physical meaning of the second term $G(\phi)$ in the right hand side of Eq. (A.10) can be easily understood on the free energy diagram, Fig. 11. At first, by putting $x \rightarrow +\infty$ in Eq. (A.10) we obtain $f_c^e = [f^L(c_L^e) - f^S(c_S^e)] / (c_L^e - c_S^e)$ because $\phi \rightarrow 0$, $d\phi/dx \rightarrow 0$, $f \rightarrow f^L(c_L^e)$ and $c \rightarrow c_L^e$ at $x \rightarrow +\infty$.

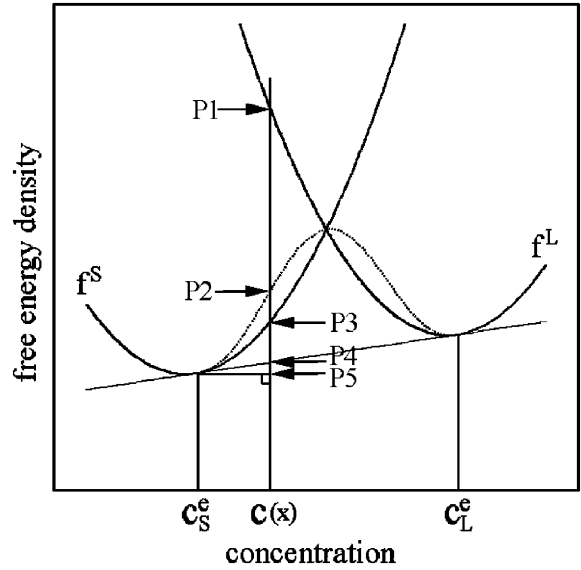


Fig. 11. Schematic curves of free energy densities of solid and liquid phases against composition.

Thus f_c^e is the slope of the common tangent line in Fig. 11. The value of the term $(c - c_S^e)f_c^e$ in Eq. (A.10) corresponds to the length between P4 and P5. The term $f - f^S(c_S^e)$ corresponds to the distance between P2 and P5. Thus $G(\phi)$, given by the distance between P2 (dotted line) and P4 (common tangent line), has a maximum value at a point within the interface region, with a vanishing value at both boundaries. Therefore it can be regarded as an extra double-well potential originating from the definition (A.4) of the free energy density at the interfacial region. It should be noted that this potential is independent of the intentionally imposed double-well potential $\omega g(\phi)$ in a standard PFM. The magnitude of the extra potential is only dependent on the free energy densities of solid and liquid phases and therefore on alloy system and temperature. If we adopt the equal chemical potential condition (2.5), instead of the equal composition condition (2.6) or (A.3), then the free energy density at an equilibrium state is given by

$$f = h(\phi)f^S(c_S^e) + [1 - h(\phi)]f^L(c_L^e), \quad (A.11)$$

because $c_S = c_S^e$ and $c_L = c_L^e$ at the equilibrium state, as shown in Section 2.3. This free energy

density represents the common tangent line itself in Fig. 11, and the extra potential disappears.

The existence of the extra potential under condition (2.6) or (A.3) imposes a restriction on the interface energy and width. The restriction condition can be derived as follows; From Eq. (A.10), we find the interface width 2ξ and interface energy

$$2\xi = \frac{\varepsilon}{\sqrt{2}} \int_{\phi_a}^{\phi_b} \frac{d\phi}{\sqrt{\omega g(\phi) + G(\phi)}}, \quad (\text{A.12})$$

$$\begin{aligned} \sigma &= \varepsilon^2 \int_{-\infty}^{+\infty} \left(\frac{d\phi}{dx} \right)^2 dx \\ &= \sqrt{2\varepsilon} \int_0^1 \sqrt{\omega g(\phi) + G(\phi)} d\phi, \end{aligned} \quad (\text{A.13})$$

where the interface width was defined to be the length of the region over which the phase field changes from ϕ_a to ϕ_b . At the sharp interface limit where $2\xi \rightarrow 0$, keeping σ constant, the extra potential $G(\phi)$ can be ignored in Eqs. (A.12) and (A.13) because ω becomes infinite. When the interface width is finite as in usual numerical computations, however, ω should be finite, and the interface width and energy are influenced by the extra potential $G(\phi)$. It can be noticed that the interface energy as well as the interface width varies with temperature because the equilibrium compositions in $G(\phi)$ are functions of temperature. Also Eqs. (A.12) and (A.13) indicate that the function $\omega g(\phi) + G(\phi)$ should be always positive at $0 < \phi < 1$. This requires $\omega > 0$, as long as we do not take $g(\phi) = G(\phi)$ as in usual cases. The condition $\omega > 0$ imposes a restriction on the interface energy as

$$\sigma \geq 4\xi \frac{\int_0^1 \sqrt{G(\phi)} d\phi}{\int_{\phi_a}^{\phi_b} 1/\sqrt{G(\phi)} d\phi}. \quad (\text{A.14})$$

The right hand side of this inequality can be regarded as the contribution of the extra double-well potential to the interface energy, which is proportional to the interface width 2ξ . This contribution becomes significant with increasing the height of the potential. The height of the extra potential is expected to increase with increasing concentration for a dilute alloy, with decreasing temperature and with decreasing partition coefficient.

An extreme case can be found when the solid is a stoichiometric phase with vanishing solubility. In this case, the free energy curve of the phase may be represented as a vertical straight line, and the height of the potential $G(\phi)$ and its contribution to the interface energy is expected to be infinite as long as the interface width remains finite.

When the interface energy is given for an alloy, inequality (A.14) imposes a restriction on the interface width too. Here we derive the restriction explicitly. Let us consider the equilibrium state having a flat boundary between S ($\phi_1 = 1$) at $x < 0$ and L ($\phi_3 = 1$) at $x > 0$, as before. For convenience we assume $T = T_E$, and so $c_L^e = c_E$ and $c_S^e = kc_E$, where k is the partition coefficient. We employ the chemical potentials (2.71)–(2.74);

$$\begin{aligned} \mu_A^S &= -\frac{RT_E}{v_m} [c_E(1-k) + c]; & \mu_A^L &= -\frac{RT_E}{v_m} c; \\ \mu_B^S &= \frac{RT_E}{v_m} \ln \frac{c}{k}; & \mu_B^L &= \frac{RT_E}{v_m} \ln c, \end{aligned} \quad (\text{A.15})$$

where we used the equal composition condition (A.3). In order to find the composition profile across the interface, we use

$$\begin{aligned} f_{cc} &= h(\phi) f_{cc}^S + [1 - h(\phi)] f_{cc}^L \\ &= h(\phi) \frac{\partial}{\partial c} (\mu_B^S - \mu_A^S) + [1 - h(\phi)] \frac{\partial}{\partial c} (\mu_B^L - \mu_A^L) \\ &= \frac{RT_E}{v_m} \left(\frac{1}{c} + 1 \right), \end{aligned} \quad (\text{A.16})$$

$$\begin{aligned} f_{c\phi} &= h'(\phi) (f_c^S - f_c^L) \\ &= h'(\phi) [\mu_B^S - \mu_A^S - \mu_B^L + \mu_A^L] \\ &= \frac{RT_E}{v_m} [c_E(1-k) - \ln k] h'(\phi). \end{aligned} \quad (\text{A.17})$$

From Eq. (A.7), therefore, the concentration profile $c(\phi)$ across the interface is found as

$$c + \ln c = c_E + \ln c_E + [-c_E(1-k) + \ln k] h(\phi). \quad (\text{A.18})$$

In order to find the $G(\phi)$ in Eq. (A.10), we use

$$f_c^e = \frac{f^L(c_E) - f^S(kc_E)}{c_E(1-k)} = \frac{RT_E}{v_m} (\ln c_E + c_E), \quad (\text{A.19})$$

$$f^S(c_S^e) - c_S^e f_c^e = -\frac{RT_E}{v_m} c_E, \quad (\text{A.20})$$

$$\begin{aligned}
f - cf_c^e &= h(\phi)f^S(c) + [1 - h(\phi)]f^L(c) - cf_c^e \\
&= h(\phi)[\mu_A^S(1 - c) + \mu_B^S c] \\
&\quad + [1 - h(\phi)][\mu_A^L(1 - c) + \mu_B^L c] - cf_c^e \\
&= -\frac{RT_E}{v_m}[c + c_E(1 - k)h(\phi)]. \quad (\text{A.21})
\end{aligned}$$

In deriving Eq. (A.21) we used Eq. (A.18). Thus, the extra-potential is given by

$$\begin{aligned}
G(\phi) &= f(c(\phi), \phi) - f^S(c_S^e) - [c(\phi) - c_S^e]f_c^e \\
&= \frac{RT_E}{v_m}[c_E - c - c_E(1 - k)h(\phi)]. \quad (\text{A.22})
\end{aligned}$$

If we take the dilute solution approximation, it follows

$$c = c_E k^{h(\phi)}, \quad (\text{A.23})$$

and

$$G(\phi) = \frac{RT_E}{v_m} c_E [1 - k^{h(\phi)} - (1 - k)h(\phi)]. \quad (\text{A.24})$$

This potential satisfies $G(0) = 0$ and $G(1) = 0$, and has a peak at

$$h(\phi) = \frac{1}{\ln k} \ln \left(\frac{k - 1}{\ln k} \right), \quad (\text{A.25})$$

for example, at $h(\phi) = 0.49$ for $k = 0.75$ and $h(\phi) = 0.41$ for $k = 0.1$. As expected, one can see that $G(\phi)$ disappears either at $c_E \rightarrow 0$ or $k \rightarrow 1$. We can directly evaluate the restriction condition (A.14) by using the potential (A.24). With the material's parameters shown in Section 3, $h(\phi) = \phi$, $\phi_a = 0$ and $\phi_b = 1$, Eq. (A.14) yields the condition $2\xi \leq 0.23 \mu\text{m}$. When the interfacial region is resolved with seven grids as in Section 3, the condition corresponds to the grid size restriction; $\Delta x \leq 0.033 \mu\text{m}$. As mentioned in Section 3, however, we adopted $\Delta x = 0.2 \mu\text{m}$ in the present computations using the equal chemical potential condition (2.5). The computation time scales as $\sim \Delta x^5$ for the directional eutectic solidification [21]. If we adopted the equal composition condition, therefore, it is expected to take much longer computational time by over thousands times than this study.

Appendix B. Chemical potential jump at interface

The chemical potential jump at the interface can be quantitatively estimated with the help of Fig. 2. If we define a function

$$Q(\phi) = \frac{D_L[1 - h(\phi)]}{D(\phi)[1 - (1 - k_1)h(\phi)]}, \quad (\text{B.1})$$

then it follows that $Q(\phi) \rightarrow 0$ at $x \rightarrow -\xi$ and $Q(\phi) \rightarrow 1$ at $x = \xi$, where we omitted the subscript under ϕ . From the $c_3(x)$ given by Eq. (2.84), we can extract the straight part $\tilde{c}_3(x)$;

$$\begin{aligned}
\tilde{c}_3(x) &= c_3^* - c_{31}^e(1 - k_1) \frac{V}{D_L} \left[\int_{-\xi}^0 Q(\phi) dx \right. \\
&\quad \left. + x - \int_0^{\xi} (1 - Q(\phi)) dx \right], \quad (\text{B.2})
\end{aligned}$$

which is the dotted straight line shown at the righthand side of Fig. 2. If we denote the intersection point between two dotted lines in Fig. 2 as $x = \delta x$, the condition $\tilde{c}_3(\delta x) = c_3^*$ yields

$$\delta x = \int_{-\xi}^0 Q(\phi) dx - \int_0^{\xi} [1 - Q(\phi)] dx. \quad (\text{B.3})$$

With $D(\phi) = D_L$ and $h(\phi) = \phi$ used in our computations, we find

$$\delta x = \int_{-\xi}^0 \frac{1 - \phi}{1 - (1 - k_1)\phi} dx - \int_0^{\xi} \frac{k_1 \phi}{1 - (1 - k_1)\phi} dx. \quad (\text{B.4})$$

Because Eqs. (2.33) and (2.35) give the equilibrium phase-field profile

$$\phi = \frac{1}{2} \left(1 - \sin \frac{\pi}{2\xi} x \right), \quad (\text{B.5})$$

Eq. (B.4) can be written as

$$\begin{aligned}
\frac{\pi \delta x}{2\xi} &= \int_{-\pi/2}^0 \frac{1 + \sin y}{2 - (1 - k_1)(1 - \sin y)} dy \\
&\quad - \int_0^{\pi/2} \frac{k_1(1 - \sin y)}{2 - (1 - k_1)(1 - \sin y)} dy. \quad (\text{B.6})
\end{aligned}$$

The integration of this equation yields δx , which is varying with the partition coefficient k_1 . From this equation one can see that δx is vanishing at $k_1 \rightarrow 1$ and increases with decreasing k_1 . For α -L interface in CBr_4 - C_2Cl_6 alloy where $k_1 = 0.75$, we get $\delta x/2\xi = 0.035$. The composition jump Δc at

$x = \delta x$ can be estimated as

$$\begin{aligned}\Delta c &= \tilde{c}_3(0) - c_3^* \\ &= \frac{d\tilde{c}_3}{dx}\delta x \\ &= c_{31}^e(1 - k_1)\frac{V}{D_L}\delta x \\ &= 0.07\tilde{\zeta}c_{31}^e(1 - k_1)\frac{V}{D_L},\end{aligned}\quad (\text{B.7})$$

which can be linked to the jump in chemical potential. With the parameters shown in Section 3, we get $\Delta c \simeq 5 \times 10^{-6}$. Also we can estimate the composition shift originating from the interface curvature, given by

$$\Delta c_k = \frac{v_m(1 - k_1)\sigma_{31}}{RT_E r}. \quad (\text{B.8})$$

With $r \simeq 5 \times 10^{-6}$ m which may be the typical radius of the interface curvature in our computations, Eq. (B.8) yields $\Delta c_k \simeq 2 \times 10^{-4}$, which is much larger than the composition jump Δc by 40 times. Thus the effect of composition jump at the α - L interface on the pattern formation is expected to be negligible in our computation conditions. By the similar way it can be shown that the effect at the β - L interface also is negligible. This rather fortunate situation is due to the k_1 and k_2 values not far from unit. If we had $k_1 = 0.01$, the composition jump at the interface may increase by about ten times to make it comparable with the curvature effect. In the phase-field equation with a temperature gradient G as in this study, the composition jump can make an extra undercooling given by $G\delta x$. However it is easy to see that this undercooling is also negligible compared with the curvature undercooling in our computations.

References

- [1] J.S. Langer, *Directions in Condensed Matter*, World Scientific, Singapore, 1986, p. 164.
- [2] G. Caginalp, *Phys. Rev. A* 39 (1989) 5887.
- [3] R. Kobayashi, *Physica D* 63 (1993) 410.
- [4] J.B. Collins, H. Levine, *Phys. Rev. B* 31 (1985) 1669.
- [5] G.B. McFadden, A.A. Wheeler, R.J. Braun, S.R. Coriell, R.F. Sekerka, *Phys. Rev. E* 48 (1993) 2016.
- [6] A.A. Wheeler, B.T. Murray, R.J. Schaefer, *Physica D* 66 (1993) 243.
- [7] O. Penrose, P.C. Pife, *Physica D* 43 (1990) 44.
- [8] A.A. Wheeler, W.J. Boettinger, G.B. McFadden, *Phys. Rev. A* 45 (1992) 7424.
- [9] J.A. Warren, W.J. Boettinger, *Acta Metall. Mater.* 43 (1995) 689.
- [10] S.G. Kim, W.T. Kim, T. Suzuki, *Phys. Rev. E* 60 (1999) 7186.
- [11] A. Karma, W.J. Rappel, *Phys. Rev. Lett.* 77 (1996) 4050.
- [12] A. Karma, W.J. Rappel, *Phys. Rev. E* 53 (1996) R3017.
- [13] A. Karma, W.J. Rappel, *Phys. Rev. E* 57 (1998) 4323.
- [14] A.A. Wheeler, G.B. McFadden, J.B. Boettinger, *Proc. R. Soc. Lond. A* 452 (1996) 495.
- [15] B. Nestler, A.A. Wheeler, *Physica D* 138 (2000) 114.
- [16] T.S. Lo, A. Karma, M. Plapp, *Phys. Rev. E* 63 (2001) 031504.
- [17] A. Karma, *Phys. Rev. E* 49 (1994) 2245.
- [18] K.R. Elder, F. Drolet, J.M. Kosterlitz, M. Grant, *Phys. Rev. Lett.* 72 (1994) 677.
- [19] F. Drolet, K. R. Elder, M. Grant, J.M. Kosterlitz, *Phys. Rev. E* 61 (2000) 6705.
- [20] K.R. Elder, M. Grant, N. Provatas, J.M. Kosterlitz, *Phys. Rev. E* 64 (2001) 021604.
- [21] M. Plapp, A. Karma, *Phys. Rev. E* 66 (2002) 061608.
- [22] I. Steinbach, F. Pezzolla, B. Nestler, M. See elberg, R. Prieler, G.J. Schmitz, J.L.L. Rezenda, *Physica D* 94 (1996) 135.
- [23] I. Tiaden, B. Nestler, H.J. Diepers, I. Steinbach, *Physica D* 115 (1998) 73.
- [24] S.G. Kim, W.T. Kim, T. Suzuki, *Phys. Rev. E* 58 (1998) 3316.
- [25] G. Faivre, J. Mergy, *Phys. Rev. E* 46 (1992) 963.
- [26] J. Mergy, G. Faivre, R. Mellet, *J. Crystal Growth* 133 (1993) 353.
- [27] G. Faivre, *J. Crystal Growth* 166 (1996) 29.
- [28] M. Ginibre, S. Akamatsu, G. Faivre, *Phys. Rev. E* 56 (1997) 780.
- [29] I. Steinbach, F. Pezzolla, *Physica D* 134 (1999) 385.
- [30] R.F. Almgren, *SIAM J. Appl. Math.* 59 (1999) 2086.
- [31] A. Karma, *Phys. Rev. Lett.* 87 (2001) 115701.
- [32] P.W. Voorhees, S.R. Coriell, G.B. McFadden, R.F. Sekerka, *J. Crystal Growth* 67 (1984) 425.
- [33] A. Karma, *Phys. Rev. Lett.* 59 (1987) 71.
- [34] K. Kassner, C. Misbah, *Phys. Rev. Lett.* 66 (1991) 445.
- [35] A. Valance, C. Misbah, D. Temkin, K. Kassner, *Phys. Rev. E* 48 (1993) 1924.
- [36] R. Bauman, K. Kassner, C. Misbah, D. Temkin, *Phys. Rev. Lett.* 74 (1995) 1597.
- [37] A. Karma, A. Sarkissian, *Metall. Mater. Trans. A* 27 (1996) 635.
- [38] K.A. Jackson, J.D. Hunt, *Trans. Metall. Soc. AIME* 236 (1966) 1129.
- [39] S. Akamatsu, M. Plapp, G. Faivre, A. Karma, *Phys. Rev. E* 66 (2002) 030501.
- [40] W.T. Kim, S.G. Kim, J.S. Lee, T. Suzuki, *Metall. Mater. Trans.* 32A (2001) 961.